Journal of Volcanology and Geothermal Research 331 (2017) 64–78

Contents lists available at ScienceDirect

Journal of Volcanology and Geothermal Research

journal homepage: www.elsevier.com/locate/jvolgeores

Geochronologic and geochemical constraints of the petrogenesis of Permian mafic dykes in the Wuding area, SW China: Implications for Fe–Ti enrichment in mafic rocks in the ELIP

Hong-Peng Fan, Wei-Guang Zhu *, Zhong-Jie Bai, Yi-Jin Yang

State Key Laboratory of Ore Deposit Geochemistry, Institute of Geochemistry, Chinese Academy of Sciences, 99 West Lincheng Road, Guiyang 550081, China

ARTICLE INFO

Article history:
Received 26 August 2016
Received in revised form 9 December 2016
Accepted 12 December 2016
Available online 19 December 2016

Keywords:
Mafic dykes
Baddeleyite geochronology
Fe–Ti enrichment
ELIP
Yangtze Block

ABSTRACT

Mafic dykes are widely distributed and well preserved in the Wuding area, SW China. The dykes are composed of fine-grained diabases, which are further subdivided into two groups (Group I and Group II). The rocks from Group I have relatively higher MgO (4.95–6.16 wt%) and lower TiO_2 (2.26–2.78 wt%) contents than those from the Group II rocks (MgO = 4.04–4.58 wt%; TiO_2 = 4.09–4.55 wt%). Two baddeleyite ages of 264 ± 3 Ma and 256 ± 5 Ma from the Wuding dykes suggest that the ages of these dykes are similar to the plutonic bodies and the associated volcanic rocks of the Emeishan large igneous province (ELIP). The compositions and isotopic signatures of the dykes are also similar to those of the ELIP volcanic rocks, indicating derivation from the same magmatic event at ~260 Ma. The primary melts of the Wuding dykes were originated by partial melting of a long-term depleted OIB-like mantle source. The Group I dykes were mainly formed by wallrock assimilation and fractional crystallization processes. The magmas parental to the Group II rocks were much more evolved than the magma parental to the Group I rocks and probably produced by wallrock assimilation and fractional crystallization of the parent magma of the Group I rocks. The increasing enrichment of Fe and Ti from the Group I to the Group II rocks were attributed to a fractional crystallization process which may be an epitome of enrichment of Fe and Ti in the Fe–Ti rich mafic intrusions of the ELIP.

1. Introduction

The ~260 Ma Emeishan large igneous province (ELIP) is an important geological feature of SW China because it hosts a number of world-class orthomagmatic Fe–Ti–V oxide deposits and series of smaller economically important Ni–Cu–(PGE) sulfide deposits (Ali et al., 2005; Zhou et al., 2008; Munteanu et al., 2013; Shellnutt, 2014). There is an extensive literature on the petro-chemical features of the Emeishan basalts (see Shellnutt, 2014 and references therein) which are further divided into two chemical groups: low-Ti and high-Ti (e.g., Xu et al., 2001; Xiao et al., 2004; Ali et al., 2005; Zhou et al., 2005, 2008). The low-Ti basaltic magmas were proposed to be generated by a relatively high degree of melting of a Fe-poor, depleted mantle source (Xu et al., 2001; Zhou et al., 2008). These magmas, being relatively dense, could have been trapped in deeper zones of the crust and could have attained sulfide saturation and generated the Ni–Cu–(PGE)-rich ultramafic intrusions (Tao et al., 2007; Zhou et al., 2008). In contrast, the high-Ti basaltic magmas would have resulted from low degrees of melting of an undepleted mantle source (Xu et al., 2001; Zhou et al., 2008). As they had a higher content of volatiles, the high-Ti basaltic magmas would have been of lower density and could have reached shallower levels in the crust, where they differentiated and produced the oxide-bearing intrusions and the alkaline intrusions (Shellnutt et al., 2011).

In the Panxi region, there are abundant ultramafic–mafic dykes in association with flood basalts and layered intrusions. Previous studies have paid some attention to these mafic dykes (e.g., Shellnutt et al., 2008, 2012; Shellnutt and Jahn, 2011), however, there is a lack of systematic and comparative studies for the region. Furthermore, the petrogenesis and mantle source characteristics of these dykes and their relationship with the Fe–Ti mineralized gabbroic intrusions especially during the subsequent processes (i.e. fractional crystallization) have not been well constrained. The detailed geochemical compositions of the original parental liquid for the high Fe–Ti gabbroic intrusions are largely speculative because the chilled margins are not commonly exposed or have been modified by magma-country rock interactions. In addition, considering the cumulate nature of the intrusive mafic-ultramafic rocks, the elemental or oxide concentrations are not useful for chemical discrimination as they would have been influenced by the selective accumulation of crystals and the removal of trapped melt from the cumulates. In most cases the parental liquids for the high Fe–Ti gabbroic intrusions are considered to be high-Ti basaltic magma (Ali et al., 2005; Zhou et al., 2008; Munteanu et al., 2013). The

* Corresponding author.
E-mail address: zhuweiguang@vip.gyig.ac.cn (W.-G. Zhu).

http://dx.doi.org/10.1016/j.jvolgeores.2016.12.005
0377-0273/

mechanisms by which such large amounts of Fe–Ti oxides accumulated in the layered intrusions in the Panxi region are still a matter of debate.

In this paper, we present two groups of mafic dykes that characterized by various enrichment of Fe and Ti (Group I: 4.95–6.16 wt% MgO, 2.26–2.78 wt% TiO_2; Group II: 4.04–4.58 wt% MgO, 4.09–4.55, see Section 4.2.1), which offer a better chance of investigating the concentrating processes of Fe and Ti in the mafic rocks of the Panxi region. Therefore, we investigate the baddeleyite U–Pb ages, and elemental and Sr–Nd isotopic geochemistry of the Wuding mafic dykes. The purposes of this study are to assess the origin and nature of the dykes, and to model the enrich processes of Fe and Ti in magmas parental to these dykes.

2. Geological background and petrography

The regional geology of the Panxi region has been described in detailed in previous studies (e.g., Chung and Jahn, 1995; Xu et al., 2001, 2007; Xiao et al., 2004; Zhang et al., 2006, 2008). The Panxi region is located in the western margin of the Yangtze Block, to the east of Tibetan plateau. The basement of the Yangtze Block comprises the Paleo–Mesoproterozoic Huili Group or its equivalents, the Kunyang and Yanbian Groups, which consist of low-grade metasedimentary rocks interbedded with felsic and mafic metavolcanic rocks, and the Neoproterozoic Kangding Complex, composed of granites and metamorphic rocks. The western margin of the Yangtze Block is marked by abundant Neoproterozoic igneous rocks, consisting dominantly of mid–Neoproterozoic felsic intrusive and volcanic rocks, and minor mafic/ultramafic rocks, including basaltic lava, sills, dikes and small intrusions (e.g., Li et al., 2003, 2006; Zhou et al., 2006a; Zhu et al., 2008). The basement is overlain by a thick sequence (>9 km) of Sinian (610–850 Ma) to Permian strata composed of clastic, carbonate, and meta-volcanic rocks (Shellnutt, 2014).

The late Permian Emeishan continental flood basalts overlying the Middle Permian limestone are exposed >5×10^5 km^2 in the western Yangtze Block (Xiao et al., 2004). Xu et al. (2001) divided the Emeishan basalts into high-Ti (>2.5 wt%) group and low-Ti (<2.5 wt%) group. As

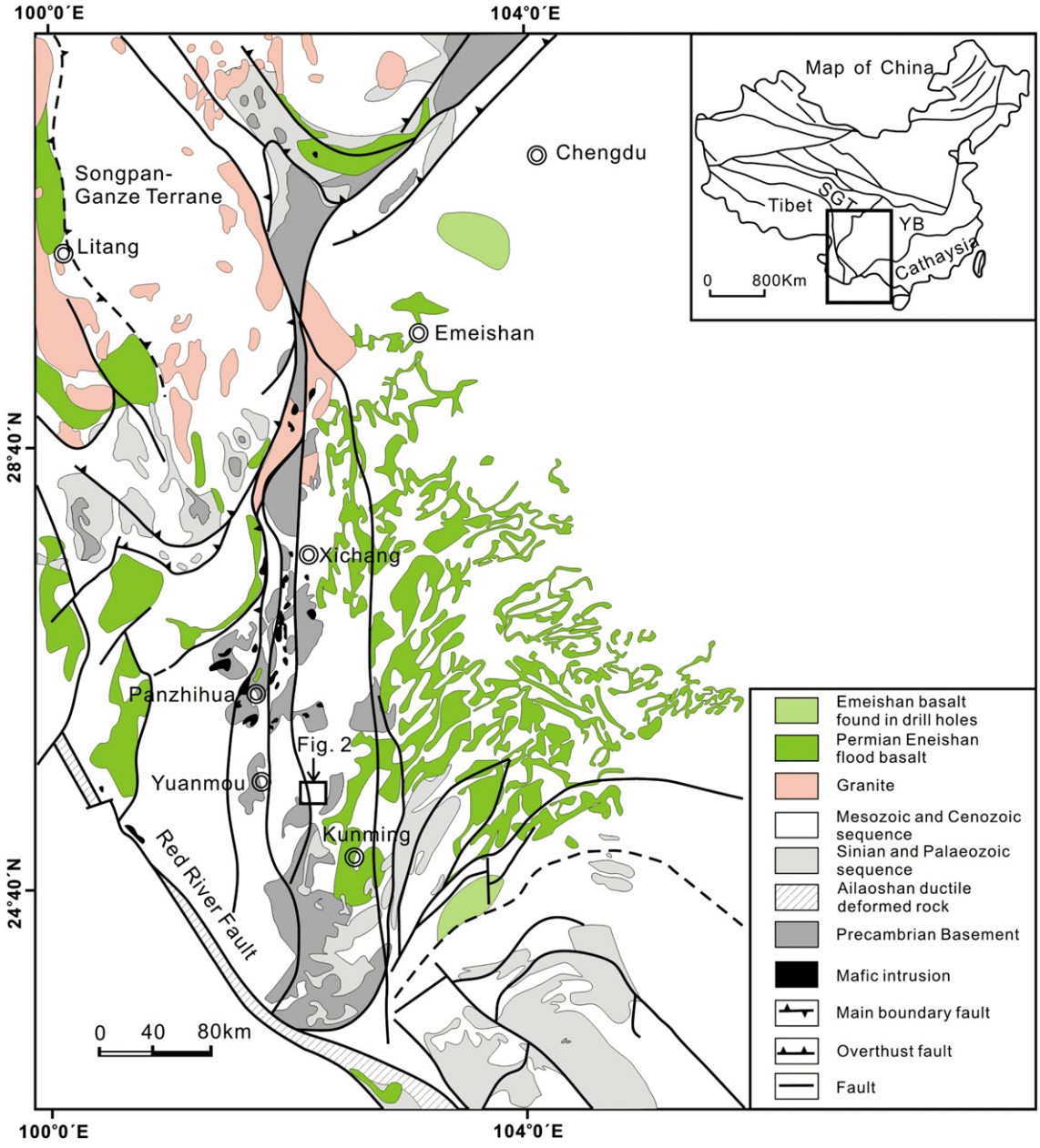

Fig. 1. Regional geological map of the Emeishan large igneous province, South China (modified from Zhou et al., 2002). SGT = Songpan–Ganze Terrane; YB = Yangtze Block.

suggested by Xu et al. (2001), the magmas parental to low-Ti group basalts were produced by larger degree (16%) of partial melting in the plume axis region which has a higher geotherm and thinner lithosphere, whereas, the magmas parental to the high-Ti group rocks were generated by lower degree (1.5%) of partial melting of the mantle at the plume periphery because of the lower temperature and thicker lithosphere. However, according to more recent studies, both the high-Ti and the low-Ti basalts were likely to be generated by partial melting of the mantle in the plume axis (e.g., Zheng et al., 2010; Anh et al., 2011).

Abundant mafic–ultramafic layered intrusions hosting several world-class Fe–Ti oxide deposits and some relatively small Cu–Ni–(PGE) sulfide deposits or mineralization are exposed in the Panxi region, including the Hongge, Xinjie, and Limahe mafic–ultramafic intrusions and the Panzhihua, Baima and Taihe mafic intrusions. The distribution of these intrusions is roughly controlled by north–south-trending faults (Fig. 1). Numerous U–Pb zircon dating results show that the mafic–ultramafic layered intrusions were emplaced at ~260 Ma and are considering part of the ELIP (Zhou et al., 2002, 2005, 2008; Zhong and Zhu, 2006). The mafic–ultramafic layered intrusion hosting giant Fe–Ti oxide deposits (e.g., Hongge, Xinjie, Baima and Panzhihua) are genetically related to the high-Ti basalt, whereas the relatively small mafic–ultramafic intrusions containing Cu–Ni–(PGE) sulfide deposits (e.g., Jinbaoshan) are associated with the low-Ti basalt (Tao et al., 2007; Zhou et al., 2008).

Late Permian mafic dykes are widely distributed in the ELIP, consisting principally of diabase, diabase prophyrite and gabbro diabase (Li et al., 2015a). These mafic dykes typically have average widths of tens of meters, and mainly intrude the late Permian Emeishan flood basalts, the late Middle Permian carbonate strata (i.e., the Qixia or Maokou limestones) and/or the older Paleozoic strata. Overall, the ages of these mafic dykes are well consistent with those of the Emeishan basalts. Recently, fresh outcrop of mafic dykes in the Wuding area were exposed by road construction. These dykes are ~150 m in width and ~10 km in length. The dominant trend of these dykes is nearly EW to NW (Fig. 2). These dykes intruded the Proterozoic to Devonian strata. Plagioclase and clinopyroxene are the major minerals with <5% magnetite in the samples from the Wuding dykes (Fig. 3).

3. Sampling and analytical methods

Twenty-six samples were collected from the best-exposed and least-altered outcrops of three dykes in the Wuding area (Fig. 2).

3.1. SIMS baddeleyite analyses

Baddeleyites from samples WD1401 and WD1402 were separated using conventional heavy liquid and magnetic techniques, then by handpicking under binocular microscopes. They were mounted in an epoxy resin disc, and polished and coated with gold film. Baddeleyites were documented with transmitted and reflected light micrographs as well as cathodoluminescence (CL) and backscattered electron images to reveal their external and internal structures. Baddeleyite grains U–Pb dating were conducted using a Cameca IMS 1280 ion microprobe (SIMS) at the Institute of Geology and Geophysics, the Chinese Academy of Sciences (CAS) in Beijing. Details of the analytical procedures for baddeleyite U–Pb dating can be found in Li et al. (2010). Oxygen flood that introduces oxygen into the sample chamber was used during the analyses, which not

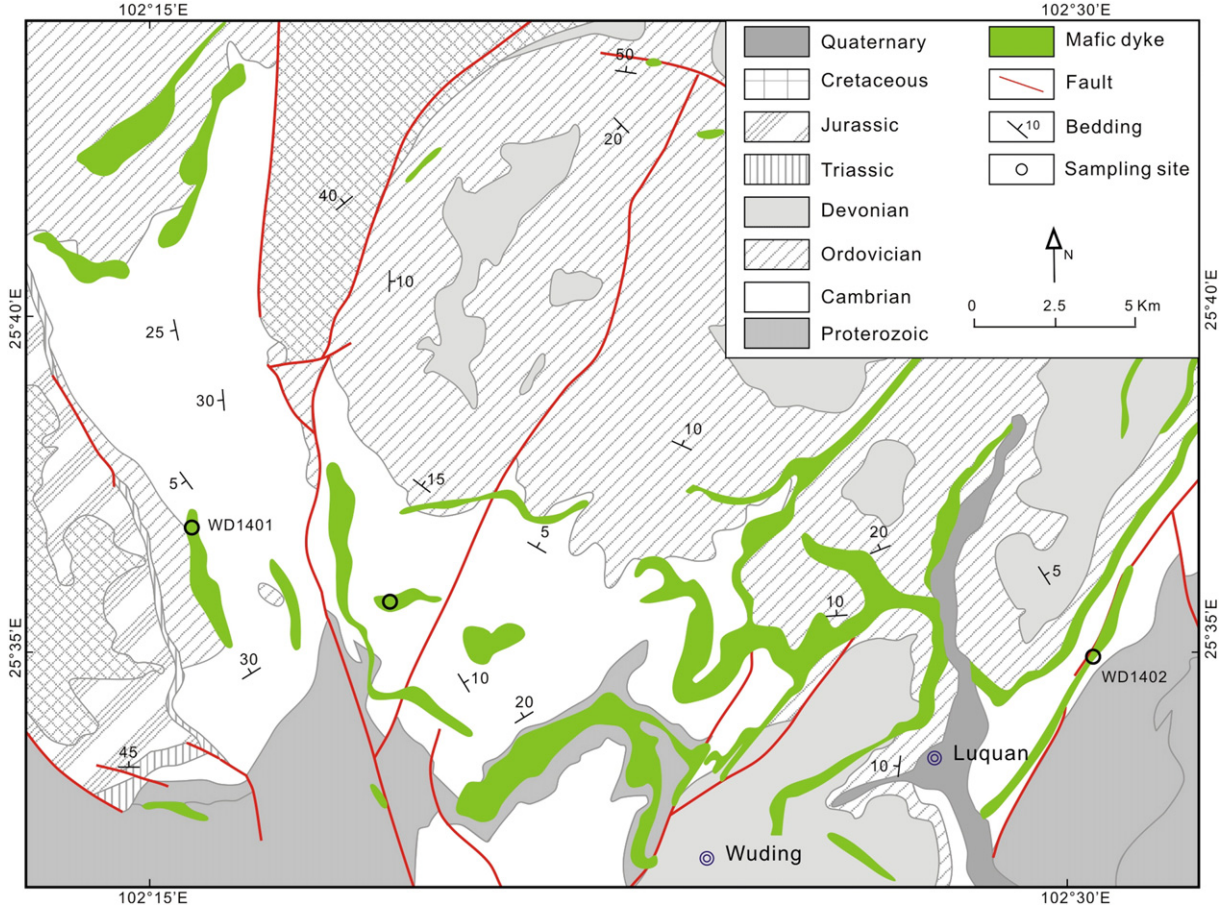

Fig. 2. Simplified geological map of the mafic dykes in the Wuding area.

only enhances Pb^+ ion yield by a factor of 7 for baddeleyite (Li et al., 2010), but also depresses the U–Pb orientation effect (Wingate and Compston, 2000) down to ~2% (Li et al., 2010). All baddeleyites were mounted in random orientations due to their small sizes and polysynthetic twinning. The weighted mean ages are quoted at the 95% confidence interval (2σ).

3.2. Whole-rock geochemical analyses

Major element compositions of whole rocks were determined using X-ray fluorescence spectrometers (XRF) at ALS Chemex Co Ltd., Guangzhou. The analytical precision was better than 5%. Trace elements in whole rocks were analyzed using a Perkin-Elmer Sciex ELAN DRC-e ICP–MS at the State Key Laboratory of Ore Deposit Geochemistry (SKLOG), Institute of Geochemistry of CAS. The powdered samples (50 mg) were dissolved with HF + HNO_3 mixture in high-pressure Teflon bombs at ~190 °C for 48 h (Qi et al., 2000). Rh was used as an internal standard to monitor signal drift during measurement. The international standards GBPG-1, OU-6, and the Chinese National standards GSR-1 and GSR-3, were used for analytical quality control. The analytical precision was generally better than 10% for trace elements.

3.3. Sr–Nd isotopic analyses

Samples for Sr–Nd isotopic analysis were spiked and dissolved with HF + HNO_3 acid in Teflon bombs. Sm and Nd were separated by conventional cation-exchange techniques. The isotopic measurements were performed on a Nu Plasma MC–ICP–MS at the State Key Laboratory of Environmental Geochemistry (SKLEG), Institute of Geochemistry of CAS. Mass fractionation corrections for Sr and Nd isotopic ratios were based on values of $^{86}Sr/^{88}Sr = 0.1194$ and $^{146}Nd/^{144}Nd = 0.7219$, respectively. Measured values for the NBS987 was $^{86}Sr/^{88}Sr = 0.710250 \pm 7$ (2σ), and for BCR-2 and JNdi-1 standards were $^{146}Nd/^{144}Nd = 0.512612 \pm 8$ (2σ) and $^{146}Nd/^{144}Nd = 0.512104 \pm 5$ (2σ), respectively.

4. Analytical results

4.1. U–Pb baddeleyite geochronology

Samples WD1401 (N 25°37′10.3″, E 102°15′20.4″) and WD1402 (N 25°35′00.1″, E 102°30′36.8″) are diabases collected from the Group I dykes and the Group II mafic dykes, respectively (Fig. 2). The SIMS baddeleyite U–Pb ages are presented in Table 1.

Baddeleyite grains from sample WD1401 are mostly anhedral, ranging from 30 to 140 μm in length, and have length to width ratios between 1:1 and 2:1. Fifteen analyses were conducted on 15 grains during a single analytical session. Measured uranium concentrations vary from 155 to 1755 ppm, and thorium contents range from 4 to 50 ppm, with Th/U ratios of 0.01–0.04 (Table 1). All 15 measurements are concordant in U–Pb isotopic systems, yielding a weighted average $^{206}Pb/^{238}U$ age of 264 ± 3 Ma (95% confidence interval, MSWD = 1.0) (Fig. 4a). This age is considered as the best estimate of the crystallization age for sample WD1401, which is interpreted to be the intrusive age of the Group I mafic dykes.

Baddeleyite grains from sample WD1402 are also mostly anhedral, ranging from 30 to 120 μm in length with length to width ratios ranging between 1:1 and 2:1. Twelve analyses give variable concentrations of U (179 to 1430 ppm) and Th (3 to 30 ppm), with Th/U ratios of 0.02–0.07 (Table 1). All the 12 analyses give concordant U–Pb results (Fig. 4b). The weighted mean $^{206}Pb/^{238}U$ age is 256 ± 5 Ma (95% confidence interval, MSWD = 1.2), which is interpreted as the best estimate of the crystallization age for sample WD1402 and the intrusive age of the Group II mafic dykes, slightly younger than the age of Group II mafic dykes (sample WD1401) (Fig. 2).

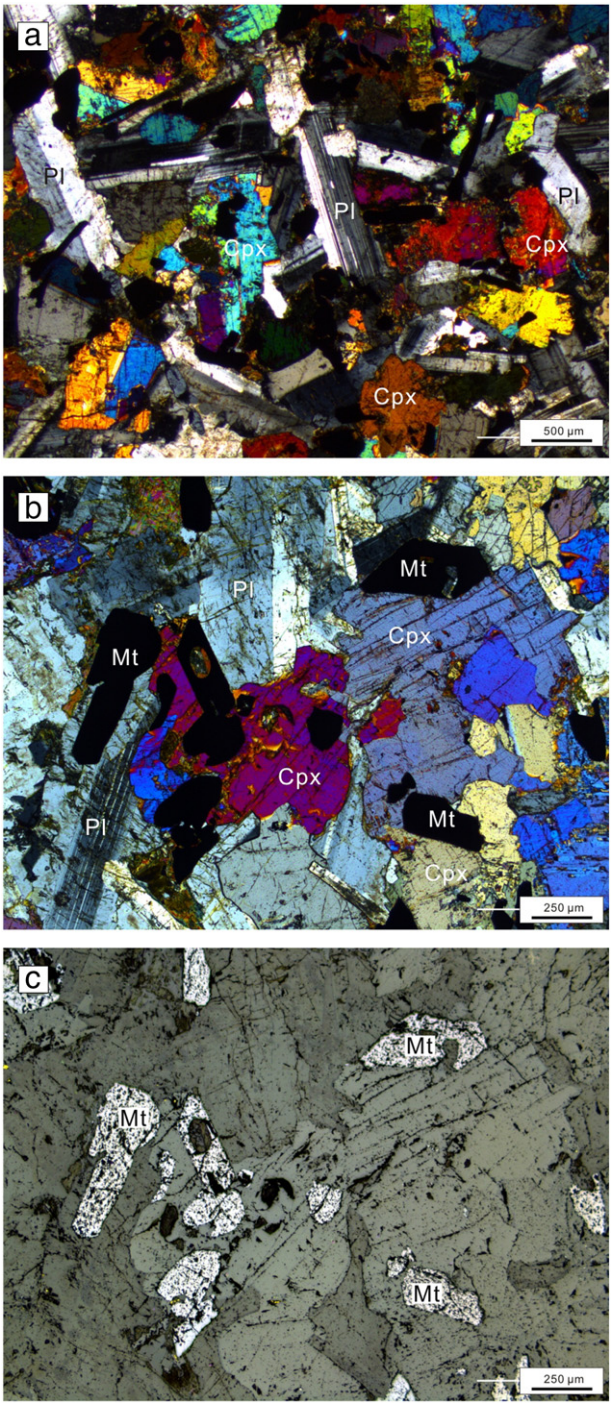

Fig. 3. Microscopic photographs of a) the Group I under transmitted light, and b) the Group II dykes under transmitted light, and c) the Group II dykes under reflected light. Pl = plagioclase; Cpx = clinopyroxene; Mt = magnetite.

4.2. Geochemical and Sr–Nd isotopic characteristics

4.2.1. Whole-rock geochemical data

Major and trace element compositions for the twenty-six samples from the mafic dykes in Wuding are presented in Table 2. The mafic dykes exhibit similar compositions with variable geochemical features. All the samples show evolved compositions with variable $Mg^{\#}$ number of 33.0–47.5 and high ratios of Ti/Y (499–746). The dykes also have highly variable MgO (4.04–6.16 wt%) and TiO_2 (2.26–4.55 wt%) (Table 2 and Fig. 5). Based on different major elemental compositions, two

Table 1
Cameca SIMS baddeleyite U–Pb isotopic analyses for the Wuding dykes.

Sample spot #	U (ppm)	Th (ppm)	Th/U	$^{206}Pb/^{204}Pb$ measured	f_{206} (%)	Isotopic ratio						Age/Ma	
						$^{206}Pb^*/^{238}U$	±1σ (%)	$^{207}Pb^*/^{235}U$	±1σ (%)	$^{207}Pb^*/^{206}Pb^*$	±1σ (%)	$^{207}Pb^*/^{206}Pb^*$ ± 1σ	$^{206}Pb^*/^{238}U$ ± 1σ
WD1401 baddeleyite (N 25°37′10.3″, E 102°15′20.4″) from Group I													
1	1110	38.9	0.035	10,380	0.18	0.0432	2.56	0.31018	2.70	0.05202	0.86	286 ± 20	273 ± 7
2	1634	12.2	0.007	18,580	0.10	0.0416	2.56	0.29687	2.74	0.05173	0.98	273 ± 22	263 ± 7
3	1080	27.1	0.025	8411	0.22	0.0415	2.56	0.28842	2.90	0.05035	1.37	211 ± 31	262 ± 7
4	415	4.38	0.011	41,469	0.05	0.0414	2.56	0.29819	3.29	0.05223	2.06	295 ± 46	262 ± 7
5	599	5.80	0.010	3636	0.51	0.0401	2.56	0.27691	3.88	0.05011	2.91	200 ± 66	253 ± 6
6	155	1.72	0.011	2607	0.72	0.0398	2.57	0.27730	5.99	0.05057	5.42	221 ± 121	251 ± 6
7	672	13.7	0.020	12,099	0.15	0.0424	2.56	0.30022	2.99	0.05137	1.55	258 ± 35	268 ± 7
8	438	4.36	0.010	11,916	0.16	0.0430	2.57	0.30503	3.01	0.05142	1.56	260 ± 36	272 ± 7
9	1563	31.0	0.020	9097	0.21	0.0416	2.56	0.29322	2.85	0.05109	1.25	245 ± 29	263 ± 7
10	1132	18.3	0.016	29,112	0.06	0.0413	2.57	0.29338	2.82	0.05156	1.16	266 ± 26	261 ± 7
11	1620	35.7	0.022	6710	0.28	0.0414	2.57	0.28628	2.97	0.05014	1.49	201 ± 34	262 ± 7
12	458	4.62	0.010	4281	0.44	0.0437	2.59	0.30992	2.94	0.05143	1.38	260 ± 31	276 ± 7
13	1059	16.1	0.015	10,263	0.18	0.0419	2.56	0.29400	2.84	0.05091	1.22	237 ± 28	265 ± 7
14	795	8.82	0.011	10,480	0.18	0.0425	2.56	0.30093	3.12	0.05136	1.78	257 ± 40	268 ± 7
15	1755	49.6	0.028	20,936	0.09	0.0413	2.56	0.29109	2.66	0.05112	0.70	246 ± 16	261 ± 7
WD1402 baddeleyite (N 25°35′00.1″, E 102°30′36.84″) from Group II													
1	589	10.1	0.017	6270	0.30	0.0399	2.56	0.27618	3.35	0.05025	2.15	207 ± 49	252 ± 6
2	699	12.5	0.018	1645	1.14	0.0406	2.56	0.27119	4.67	0.04846	3.90	122 ± 89	256 ± 6
3	559	15.7	0.028	1380	1.35	0.0413	2.56	0.27997	4.96	0.04919	4.25	157 ± 97	261 ± 7
4	766	25.1	0.033	3783	0.49	0.0418	2.56	0.29250	3.41	0.05075	2.25	230 ± 51	264 ± 7
5	179	3.23	0.018	1661	1.13	0.0422	2.57	0.28622	6.23	0.04916	5.68	156 ± 128	267 ± 7
6	781	19.4	0.025	14,500	0.13	0.0401	2.83	0.28298	3.63	0.05117	2.27	248 ± 51	254 ± 7
7	1430	16.6	0.012	8747	0.21	0.0391	2.57	0.27669	3.21	0.05134	1.93	256 ± 44	247 ± 6
8	444	7.40	0.017	15,090	0.12	0.0394	2.57	0.29176	3.54	0.05376	2.43	261 ± 54	249 ± 6
9	751	50.5	0.067	6679	0.28	0.0414	2.57	0.29485	3.70	0.05170	2.66	272 ± 60	261 ± 7
10	1301	30.5	0.023	31,988	0.06	0.0424	2.71	0.30258	2.89	0.05175	1.01	274 ± 23	268 ± 7
11	421	8.80	0.021	5555	0.34	0.0403	2.56	0.29025	3.82	0.05222	2.83	295 ± 63	255 ± 6
12	749	13.2	0.018	n/a	0.00	0.0393	2.59	0.28751	3.09	0.05300	1.68	329 ± 38	249 ± 6
Phalaborwa (baddeleyite standard)													
1	283	6.41	0.023	9639	0.19	0.3466	2.83	6.06411	2.88	0.12688	0.53	2055 ± 9	1919 ± 47
2	440	8.85	0.020	209,745	0.01	0.3530	2.70	6.18727	2.77	0.12713	0.61	2059 ± 11	1949 ± 46
3	216	3.45	0.016	n/a	0.00	0.3566	2.71	6.28905	2.74	0.12791	0.45	2069 ± 8	1966 ± 46
4	465	9.21	0.020	n/a	0.00	0.3585	2.70	6.29669	2.72	0.12737	0.36	2062 ± 6	1975 ± 46
5	229	4.17	0.018	n/a	0.00	0.3603	2.71	6.33957	2.80	0.12760	0.71	2065 ± 12	1984 ± 46
6	413	7.46	0.018	n/a	0.00	0.3636	2.77	6.32662	2.79	0.12620	0.40	2046 ± 7	1999 ± 48
7	241	2.48	0.010	123,396	0.02	0.3658	2.71	6.42915	2.78	0.12747	0.61	2063 ± 11	2010 ± 47
8	221	3.68	0.017	n/a	0.00	0.3681	2.70	6.42268	2.74	0.12656	0.50	2051 ± 8	2020 ± 47
9	214	3.23	0.015	n/a	0.00	0.3702	2.70	6.53636	2.75	0.12806	0.49	2072 ± 9	2030 ± 47
10	206	3.26	0.016	n/a	0.00	0.3732	2.71	6.48632	2.78	0.12607	0.65	2044 ± 11	2044 ± 48
11	366	6.45	0.018	n/a	0.00	0.3766	2.70	6.60519	2.72	0.12720	0.35	2060 ± 6	2060 ± 48
12	356	5.86	0.016	n/a	0.00	0.3855	2.70	6.79566	2.71	0.12785	0.31	2069 ± 6	2102 ± 49
13	495	7.68	0.016	n/a	0.00	0.3887	2.74	6.79458	2.81	0.12677	0.61	2054 ± 11	2117 ± 50

Errors are 1σ; f_{206} is the percentage of common ^{206}Pb in total ^{206}Pb; Common Pb corrected using the measured ^{204}Pb. n/a, not available.

kinds of groups are classified: Group I dykes and Group II dykes. The Group I dykes have higher MgO (4.95–6.16 wt%) and lower TiO_2 (2.26–2.78 wt%) contents, whereas the Group II dykes show lower MgO (4.04–4.58 wt%) and higher TiO_2 (4.09–4.55 wt%) contents (Fig. 5), which are very similar to the HT2 and HT1 basalts from the ELIP, respectively (e.g., Xu et al., 2001). Fe_2O_3, TiO_2, P_2O_5 and total alkalis ($Na_2O + K_2O$) contents increase, whereas Al_2O_3, CaO, Cr, and V contents decrease with decreasing MgO contents of the Group I samples (Fig. 5). However, the Group II samples have relatively consistent major oxides contents except the Fe_2O_3, TiO_2, Cr and Ni contents and show some correlations with the MgO contents similar to that of the Group I samples. On the Nb/Y vs. Zr/TiO_2 diagram, these rocks from the Wuding dykes plot in the alkaline basalt field (Fig. 6).

Despite variable REE abundances, the samples from the two groups have parallel REE patterns with enrichments in light rare earth elements (LREEs) and depletions in heavy rare earth elements (HREEs) [$(La/Yb)_N$ = 7.5–10.6; subscript N denotes the chondrite-normalized] (Boynton, 1984) (Fig. 7a). Among them, the Group II samples have high total REE contents with obvious positive Eu anomalies. In the primitive mantle-normalized multi-element plot (Fig. 7b), all the samples from the Wuding mafic dykes show "humped" patterns characterized by variable enrichment in all incompatible elements with slightly negative to no obvious Nb–Ta anomalies relative to the neighboring elements, which are similar to typical intraplate alkali basaltic rocks in CFB and OIB provinces (Sun and McDonough, 1989). The Group II samples exhibit negative Ba, Sr, P and Eu anomalies (Fig. 7b).

4.2.2. Sr–Nd isotopes

Samples from the Wuding mafic dykes display variable Sr–Nd isotopic compositions (Table 3). The Group I samples have $(^{87}Sr/^{86}Sr)_I$ ratios ranging from 0.7048 to 0.7077, much more variable than that of the Group II samples (0.7054–0.7059) (Table 3). Although Sr isotopic variations can be partly due to the mobile nature of Rb and Sr during alteration, the differences between the two groups of dykes reflect their different origins or variable contaminations of crustal materials. On the other hand, the Nd isotopic compositions within the two groups are relatively constant. The $(^{143}Nd/^{144}Nd)_I$ ratios range from 0.512308 to 0.512463 for the Group I rocks and from 0.512349 to 0.512496 for the Group II rocks, corresponding to $\varepsilon_{Nd}(T)$ values ranging from 0.11 to 3.1 for the Group I rocks and from 0.87 to 3.8 for the Group II rocks, respectively. $\varepsilon_{Nd}(T)$ values show an overall negative correlation with $(^{87}Sr/^{86}Sr)_I$ ratios. All the rocks from these mafic dykes are plotted in

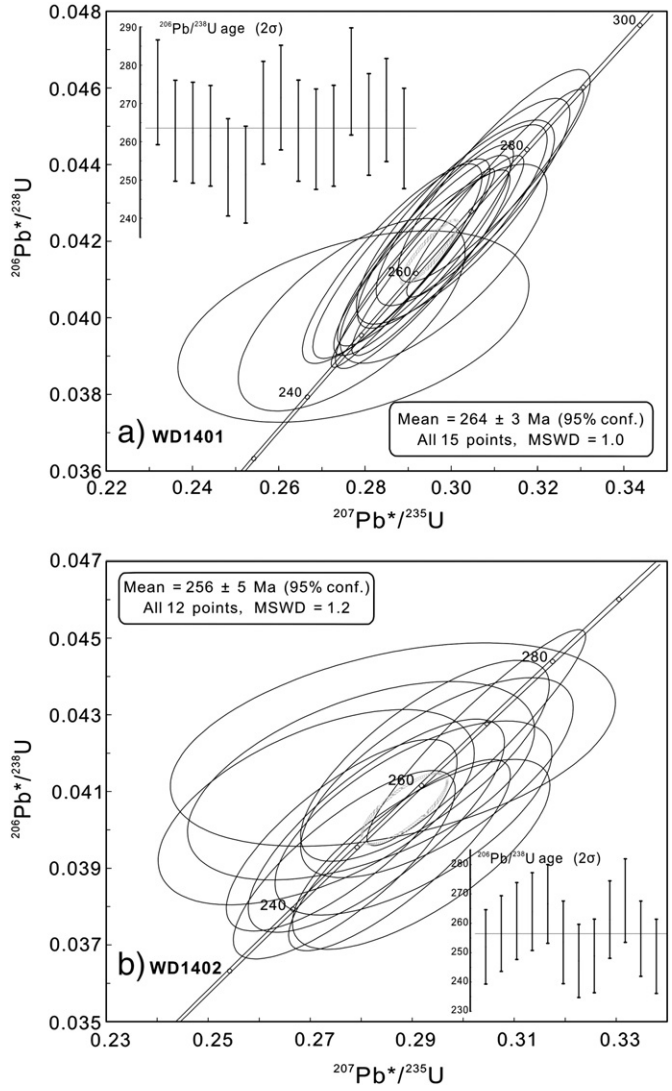

Fig. 4. Baddeleyite U–Pb concordia diagrams of sample (a) WD1401 and (b) WD1402 from the Wuding mafic dykes.

the field of the Emeishan high-Ti basalts but have a larger range than that of the other dykes in the ELIP (Fig. 8).

5. Discussion

5.1. Emplacement age of the mafic dykes

Baddeleyite has long been considered an ideal geochronometer for dating crystallization ages of mafic–ultramafic rocks by the U–Pb isotopic method, because (1) it crystallizes in the late-stage, chemically fractionated portions of mafic magmas; (2) it contains variably high U concentrations and negligible initial common Pb; (3) it rarely occurs as xenocrysts in mafic–ultramafic intrusions; and (4) it appears to be much less susceptible to Pb loss than zircon (see Rodionov et al., 2012 and references therein). Thus, the two baddeleyite ages of 264 ± 3 Ma and 256 ± 5 Ma from the Wuding dykes are probably the best estimate of the crystallization ages for these rocks.

On the basis of geological correlations, the eruption of the Emeishan flood basalts is constrained to be the late middle Permian (~260 Ma) (Yin et al. 1992; Jin and Shang, 2000). The initiation of ELIP volcanism is well constrained by both biostratigraphic and radiometric techniques. For instance, zircon U–Pb dating of plutonic rocks consistently yielded ages around 260 Ma though there are ages between 251 Ma and 255 Ma (see Shellnutt, 2014 and references therein). Moreover, dyke samples collected from the Panxi region also gave ages of ~260 Ma (e.g., Guo et al., 2004; Zhou et al., 2006b; Han et al., 2009; Shellnutt and Jahn, 2011; Li et al., 2012, 2015b). All these dating data define a rather consistent age range which was contemporaneous with the eruption of the flood basalts and the emplacement of the adjacent mafic–ultramafic layered intrusions associated with the ELIP. Late Permian mafic dykes are widely distributed in the ELIP, consisting principally of diabase, diabase prophyrite and gabbro diabase (Li et al., 2015a). These mafic dykes typically have average widths of tens of meters, and mainly intrude the late Permian Emeishan flood basalts, the late Middle Permian carbonate strata (i.e., the Qixia or Maokou limestones) and/or the older Paleozoic strata. In particular, Shellnutt et al. (2012) reported high-precision CA-TIMS zircon U–Pb ages of the Miyi mafic dykes with a narrow age range from 257 to 260 Ma, which is coincident with the major eruptive stage of the ELIP (Shellnutt, 2014). Even now mafic dykes in Wuding were not previously systematic and comprehensive studied, the baddeleyite ages presented here for the dykes are similar to the ages for the Emeishan basalts, mafic–ultramafic intrusions and granites (Zhou et al., 2002, 2005, 2008; Zhong and Zhu, 2006; Fan et al., 2004, 2008; Xu et al., 2008; Shellnutt et al., 2009; Zhong et al., 2011; Lai et al., 2012), which unequivocally indicates a temporal link with them. The geochronology of the dykes in Wuding is broadly comparable to high-Ti basalts of the ELIP elsewhere. Although the Group II mafic dykes are slightly younger than the Group I mafic dykes, it is suggested that the mafic rocks in Wuding were produced by the same mantle plume that generated the ELIP at ~260 Ma.

5.2. Petrogenesis of the Wuding mafic dykes

5.2.1. Fractional crystallization and crustal contamination

Compositional variations within the Group I and Group II rocks suggest that they have undergone similar evolutionary trends as shown by the Fenner diagrams (Fig. 5). Fractional crystallization appears to have played a major role in the compositional evolution of the Wuding mafic dykes especially the Group I dykes duo to the variable MgO, Ni and other compatible element contents and the regular variations of other elemental concentrations (Table 2).

In the Group I dykes, Fe_2O_3 and TiO_2 increase with decreasing MgO contents (Fig. 5), likely reflecting that TiO_2 was incompatible in the crystallizing phases and Fe–Ti oxides (titanomagnetite and ilmenite) did not reach the liquidus in these systems, which is consistent with the observations of thin sections (Fig. 3a). As MgO decreases, Al_2O_3 decrease slightly, Cr and Ni decreases quickly, indicating crystal fractionation of dominant olivine/clinopyroxene. The MgO decreases and TiO_2 increases quickly for the Group I dykes indicative of dominant olivine fractionation trend as the decreasing TiO_2 indicative of dominant clinopyroxene fractionation. The increasing ($K_2O + Na_2O$) contents with decreasing MgO contents (Fig. 5) plus the positive correlation of Al_2O_3 vs. MgO indicate that the mafic dykes were subjected to plagioclase fractionation. Moreover, the slightly positive anomalies of Eu (Eu/Eu* = 1.13) and Sr from the Group I rocks suggest that they have been effected by plagioclase fractional crystallization. The correlation between P_2O_5 and MgO suggests apatite did not reach the liquidus when crystallization fractionation took place.

The Group II rocks display obviously higher Fe_2O_3 and TiO_2 but lower MgO contents with much more evolved nature than that of the Group I rocks. The Group II rocks are also affected by olivine fractionation as MgO decreases, Al_2O_3 decreases slightly, Cr and Ni decrease quickly (Fig. 5). Relative consistent CaO contents (Fig. 5) imply that the magmas parental to these rocks underwent insignificant clinopyroxene fractionation. The negative anomalies of Eu and Sr from the Group II rocks are due to plagioclase fractionation (Fig. 7). In the element ratio plots of Al/K versus (2Ca + Na)/K and Si/K versus (2Ca + 3Na)/K (Fig. 9a and b), both the Group I and II dykes yield tight linear regression lines, indicating that Si, Ca, Na, and K in these samples could have been controlled by

Table 2
Major elements (in wt%) and trace elements (in ppm) data of the Wuding dykes.

Sample no.	WD1301	WD1302	WD1401	WD1410	WD1411	WD1303	WD1304	WD1305	WD 1306	WD 1307
Group	I	I	I	I	I	I	I	I	I	I
SiO_2	47.90	47.90	48.30	47.81	47.98	47.90	47.90	48.40	47.80	48.00
TiO_2	2.71	2.71	2.57	2.74	2.74	2.30	2.33	2.26	2.35	2.53
Al_2O_3	13.35	13.30	13.75	13.55	13.61	14.60	14.45	15.00	14.85	14.70
Fe_2O_3	15.06	14.79	14.24	15.13	14.89	13.55	13.68	13.30	13.38	14.02
MnO	0.25	0.23	0.22	0.23	0.23	0.20	0.21	0.20	0.20	0.21
MgO	4.83	4.85	4.97	5.00	4.88	6.11	6.07	5.90	5.81	5.54
CaO	6.70	6.87	8.23	7.56	7.86	10.65	10.65	10.70	10.60	10.45
Na_2O	2.72	2.85	3.12	3.32	3.24	2.86	2.88	2.94	2.89	2.96
K_2O	3.53	3.33	2.63	2.58	2.60	0.74	0.77	0.76	0.74	0.83
P_2O_5	0.49	0.49	0.45	0.46	0.49	0.35	0.36	0.37	0.35	0.39
LOI	1.24	1.09	1.52	1.39	1.28	0.00	0.00	0.00	0.00	0.00
Total	98.78	98.41	100.00	99.77	99.80	99.26	99.30	99.83	98.97	99.63
$Mg^{\#}$	38.8	39.4	40.87	39.6	39.4	47.2	46.8	46.77	46.2	43.9
Sc	28.7	28.5	27.5	29.6	28.2	29.6	30.2	26.8	29.4	29.6
V	303	303	191	365	340	291	298	244	297	307
Cr	38.1	40.4	37.3	36.2	28.7	99.8	99.7	96.5	95.7	88.5
Co	45.7	44.1	39.9	44.8	42.4	48.9	49.6	45.5	48.5	47.7
Ni	45.5	41.1	33.0	46.8	42.4	77.0	76.9	55.4	74.1	66.2
Cu	180.0	171.0	136.9	207.0	197.0	167.0	179.0	117.7	172.0	188.0
Zn	287	144	87.2	155	144	128	136	95.1	131	141
Ga	21.4	21.3	21.4	21.0	20.4	19.4	19.9	20.7	20.0	20.2
Rb	56.4	54.6	44.3	45.8	42.0	16.1	16.2	17.6	15.9	18.2
Sr	1710	1440	1390	1230	1280	574	586	605	582	574
Y	33.4	31.4	29.6	29.4	29.0	21.6	22.0	22.5	21.7	24.1
Zr	186	191	175	179	178	116	121	120	117	133
Nb	26.5	26.9	23.2	23.8	23.9	16.9	17.1	16.4	17.4	18.9
Cs	0.71	0.60	0.41	0.43	0.52	0.38	0.41	0.36	0.41	0.47
Ba	704	631	669	678	644	386	396	407	390	425
La	33.6	33.7	28.9	29.7	29.5	20.4	21.4	21.8	21.0	23.1
Ce	72.9	73.7	66.0	66.9	66.1	46.2	47.6	49.2	47.6	51.6
Pr	9.42	9.17	8.41	8.14	8.09	5.83	5.94	6.22	5.89	6.48
Nd	39.8	39.3	35.0	34.9	35.0	25.3	26.2	26.7	26.0	27.7
Sm	7.76	7.91	7.09	6.66	7.06	5.32	5.25	5.43	5.29	5.49
Eu	3.08	2.95	2.64	2.68	2.72	2.06	2.07	2.15	2.06	2.19
Gd	7.98	7.56	6.63	6.91	7.33	5.17	5.20	5.14	5.11	5.55
Tb	1.22	1.20	1.03	1.03	1.01	0.80	0.84	0.83	0.81	0.88
Dy	6.34	6.17	5.28	5.49	5.39	4.22	4.25	4.31	4.26	4.56
Ho	1.25	1.20	1.03	1.03	1.01	0.82	0.84	0.78	0.84	0.92
Er	3.40	3.28	2.97	2.73	2.67	2.21	2.27	2.21	2.21	2.55
Tm	0.43	0.40	0.38	0.38	0.39	0.27	0.32	0.28	0.29	0.32
Yb	2.66	2.69	2.44	2.26	2.33	1.84	1.82	1.79	1.84	1.97
Lu	0.40	0.39	0.34	0.31	0.36	0.26	0.28	0.27	0.28	0.31
Hf	4.46	4.44	3.74	3.90	3.63	2.81	2.87	2.80	2.93	3.28
Ta	1.65	1.60	1.34	1.23	1.22	1.01	1.00	0.95	1.06	1.16
Pb	5.39	5.47	4.66	4.99	4.39	2.90	2.58	2.90	2.39	3.02
Th	3.18	3.29	2.84	3.55	3.57	1.79	1.86	1.85	1.80	2.11
U	0.80	0.77	0.72	0.99	0.92	0.43	0.44	0.45	0.44	0.49
Ti/Y	499	532	528	568	575	643	639	603	656	632

Sample no.	WD1412	WD1413	WD1414	WD1415	WD 1308	WD 1309	WD1402	WD1403	WD1404	WD1405
Group	I	I	I	I	II	II	II	II	II	II
SiO_2	47.98	47.56	47.46	47.71	49.50	49.40	49.50	49.10	49.20	48.23
TiO_2	2.50	2.47	2.67	2.70	4.07	4.05	4.09	4.15	4.20	4.49
Al_2O_3	14.96	14.98	14.37	14.47	13.00	13.00	12.95	12.60	12.75	12.41
Fe_2O_3	13.74	13.64	14.36	14.36	15.32	14.96	15.84	15.74	15.82	16.31
MnO	0.21	0.20	0.21	0.22	0.18	0.18	0.20	0.21	0.21	0.21
MgO	5.90	5.84	5.74	5.75	4.47	4.53	4.04	4.15	4.16	4.15
CaO	10.71	10.74	10.42	10.48	8.22	8.34	8.17	8.18	8.31	8.30
Na_2O	3.01	2.99	3.01	3.07	2.50	2.47	2.75	2.64	2.65	2.64
K_2O	0.81	0.78	0.85	0.88	1.60	1.60	1.68	1.62	1.58	1.58
P_2O_5	0.38	0.39	0.41	0.41	0.46	0.46	0.46	0.43	0.43	0.47
LOI	0.00	0.00	0.00	0.00	0.70	0.62	0.34	0.35	0.28	0.88
Total	100.20	99.59	99.50	100.05	100.02	99.61	100.02	99.17	99.59	99.67
$Mg^{\#}$	46.0	45.9	44.2	44.2	36.6	37.5	33.6	34.3	34.2	33.5
Sc	29.3	30.1	29.0	29.7	25.8	25.0	23.9	25.2	24.0	27.9
V	342	339	346	339	345	338	234	254	247	423
Cr	87.8	88.0	82.4	78.1	67.1	65.7	10.4	18.5	8.7	10.8
Co	47.6	47.7	47.3	47.3	45.0	43.3	40.0	40.6	39.2	42.8
Ni	67.4	66.9	62.3	64.8	65.3	66.2	21.3	28.5	22.4	29.2
Cu	159.0	161.0	175.0	172.0	269	256	240	235	230	308
Zn	132	132	147	153	177	180	130	134	130	176
Ga	20.3	19.8	20.4	19.9	24.8	24.6	27.2	28.2	26.2	24.8
Rb	16.6	16.6	18.3	18.0	46.7	45.2	53.8	53.2	49.1	45.2
Sr	583	573	555	544	474	481	543	527	526	489

Table 2 (*continued*)

Sample no.	WD1412	WD1413	WD1414	WD1415	WD 1308	WD 1309	WD1402	WD1403	WD1404	WD1405
Group	I	I	I	I	II	II	II	II	II	II
Y	22.6	22.3	24.3	23.7	37.3	36.2	40.2	40.3	38.1	36.5
Zr	125	123	134	136	336	331	351	365	334	330
Nb	17.6	17.0	18.9	19.1	39.3	38.0	39.6	40.2	39.6	41.8
Cs	0.32	0.39	0.41	0.37	1.02	2.81	1.38	1.23	1.25	1.09
Ba	403	396	426	419	383	407	455	442	428	402
La	20.7	20.6	22.6	22.7	42.8	41.9	43.2	42.2	40.0	39.9
Ce	46.2	47.1	50.3	49.9	95.5	93.9	97.1	93.8	89.5	87.5
Pr	5.73	5.76	6.38	6.25	12.1	11.9	12.7	12.5	11.9	11.3
Nd	25.1	25.3	26.7	27.9	51.4	50.0	53.3	52.4	49.1	49
Sm	5.10	5.52	5.32	5.60	10.7	10.2	11.1	10.8	10.2	9.80
Eu	2.12	2.11	2.33	2.25	3.30	3.26	3.58	3.48	3.28	3.65
Gd	5.21	5.21	5.80	5.84	9.37	9.44	9.94	9.99	9.48	9.85
Tb	0.77	0.74	0.84	0.79	1.58	1.52	1.56	1.48	1.49	1.48
Dy	4.22	4.19	4.20	4.58	7.63	7.54	7.62	7.46	7.29	7.39
Ho	0.80	0.80	0.81	0.84	1.43	1.39	1.51	1.48	1.41	1.32
Er	2.12	2.03	2.34	2.17	3.91	3.78	4.07	4.03	3.96	3.73
Tm	0.31	0.26	0.30	0.26	0.47	0.50	0.49	0.50	0.48	0.47
Yb	1.79	1.54	1.79	1.83	3.08	3.00	3.14	3.05	3.01	2.97
Lu	0.23	0.24	0.23	0.24	0.43	0.43	0.45	0.44	0.40	0.38
Hf	2.63	2.69	3.07	3.06	8.49	8.14	8.06	8.51	8.05	7.78
Ta	0.87	0.86	0.99	0.98	2.41	2.34	2.36	2.42	2.46	2.38
Pb	2.77	2.58	2.95	3.03	4.25	6.03	5.90	5.67	6.10	6.13
Th	2.10	2.09	2.29	2.28	6.02	5.94	6.24	6.24	5.71	6.30
U	0.55	0.49	0.64	0.56	1.41	1.43	1.50	1.46	1.37	1.52
Ti/Y	662	667	662	682	659	677	612	625	665	746

Sample no.	WD1406	WD1407	WD1408	WD1409	WD1416	WD1417
Group	II	II	II	II	II	II
SiO_2	48.60	48.27	48.59	48.85	48.83	48.91
TiO_2	4.28	4.41	4.26	4.27	4.14	4.13
Al_2O_3	12.69	12.59	12.87	13.02	12.95	13.01
Fe_2O_3	16.00	16.41	16.11	16.11	14.63	14.78
MnO	0.20	0.22	0.21	0.21	0.18	0.15
MgO	4.02	4.09	4.01	4.04	4.32	4.23
CaO	8.26	8.38	8.38	8.28	8.03	7.92
Na_2O	2.71	2.63	2.75	2.74	2.54	2.41
K_2O	1.64	1.52	1.55	1.55	1.55	1.62
P_2O_5	0.48	0.47	0.48	0.47	0.46	0.47
LOI	0.77	0.72	0.43	0.42	2.08	2.18
Total	99.65	99.71	99.64	99.96	99.71	99.81
$Mg^{\#}$	33.2	33.0	33.0	33.2	36.9	36.2
Sc	26.7	27.1	27.1	27.7	26.0	25.5
V	416	408	401	395	373	377
Cr	9.44	8.74	9.39	7.53	54.3	57.2
Co	43.1	42.7	42.2	43.4	44.9	42.6
Ni	29.5	29.0	28.9	23.8	60.3	60.6
Cu	340	380	380	405	235	235
Zn	180	195	198	183	169	185
Ga	26.1	26.3	25.9	25.8	24.5	24.7
Rb	51.3	46.3	47.7	47.8	46.1	47.4
Sr	535	511	507	522	460	460
Y	38.4	36.9	38.1	38.0	36.2	36.6
Zr	337	326	333	340	327	336
Nb	40.7	40.5	41.0	41.5	36.9	37.5
Cs	1.18	1.31	1.27	1.18	1.09	1.13
Ba	430	395	406	407	368	376
La	43.1	39.6	41.5	41.8	39.3	40.6
Ce	97.4	92.4	92.8	92.3	88.2	90.5
Pr	12.4	11.5	11.7	11.6	10.9	11.5
Nd	54	51	50	51	48	50
Sm	10.7	10.1	10.5	9.98	9.81	10.3
Eu	3.77	3.50	3.50	3.55	3.42	3.28
Gd	11.1	10.3	10.5	10.5	9.2	10.1
Tb	1.49	1.35	1.38	1.46	1.26	1.40
Dy	7.84	7.27	7.17	7.01	6.76	7.31
Ho	1.44	1.30	1.28	1.40	1.28	1.30
Er	3.56	3.62	3.77	3.58	3.53	3.47
Tm	0.47	0.47	0.46	0.44	0.47	0.46
Yb	2.73	2.69	2.98	2.96	2.74	2.73
Lu	0.40	0.41	0.40	0.40	0.39	0.39
Hf	8.09	7.31	8.11	7.89	7.39	7.49
Ta	2.29	2.19	2.16	2.19	1.91	1.95
Pb	6.17	6.41	6.39	5.63	7.52	6.57
Th	7.29	6.65	6.78	7.00	6.55	6.81

(*continued on next page*)

Table 2 (*continued*)

Sample no.	WD1406	WD1407	WD1408	WD1409	WD1416	WD1417
Group	II	II	II	II	II	II
U	1.70	1.63	1.62	1.62	1.67	1.66
Ti/Y	676	724	676	677	702	693

$Mg^{\#} = 100 * \text{molar MgO}/(Mg + FeO_T)$, assuming $FeO^T = 0.9 * Fe_2O_3$, total iron as FeO^T. LOI = loss on ignition.

crystal separation/addition of mainly plagioclase with minor clinopyroxene (Russell and Nicholls, 1988). Moreover, the plagioclase shows an An of 60 in the plot of Al/K versus 2Na/K (Fig. 9c), which is similar to the compositions of equilibrium plagioclases for most samples calculated by using COMAGMAT–3.5 (Ariskin, 1999) (Appendix A). These results are consistent with microscopic observation, petrography and major and trace element characteristics discussed above.

In summary, olivine plus minor amounts of plagioclase are the major fractionated minerals for the Group I and the Group II dykes in the Wuding area.

The variations in the Sr–Nd isotopic compositions of the samples from the dykes may reflect the mantle source heterogeneity or different magma process. However, the scatter of both $(^{87}Sr/^{86}Sr)_I$ and $\varepsilon_{Nd}(T)$ values of these samples is in accordance with variable degrees of crustal contamination (Fig. 8). In addition, some rocks from the Group I and Group II mafic dykes are characterized by slightly negative Nb–Ta anomalies (Fig. 7b), which can be accounted for by slightly crustal contamination, because continental crust is typically depleted in Nb and Ta (Rudnick and Fountain, 1995; Rudnick and Gao, 2003). The samples with relatively higher $(^{87}Sr/^{86}Sr)_I$ ratios and lower $\varepsilon_{Nd}(T)$ values generally have lower MgO contents and Th/Nb ratios, and this warrants the speculation of the involvement of an assimilation and fractional crystallization (AFC) process which is commonly utilized to explain the geochemical differences between continental flood basalts and ocean island basalts or mid-ocean-ridge basalts. Therefore, we propose that the AFC process was involved during the evolution of magmas in the area. As shown in Fig. 10a, obvious positive correlation between Sm and Rb contents can be explained by slight wallrock assimilation and significant fractional crystallization of olivine, plagioclase, and clinopyroxene. The relative enrichment of Th and depletion of Nb and

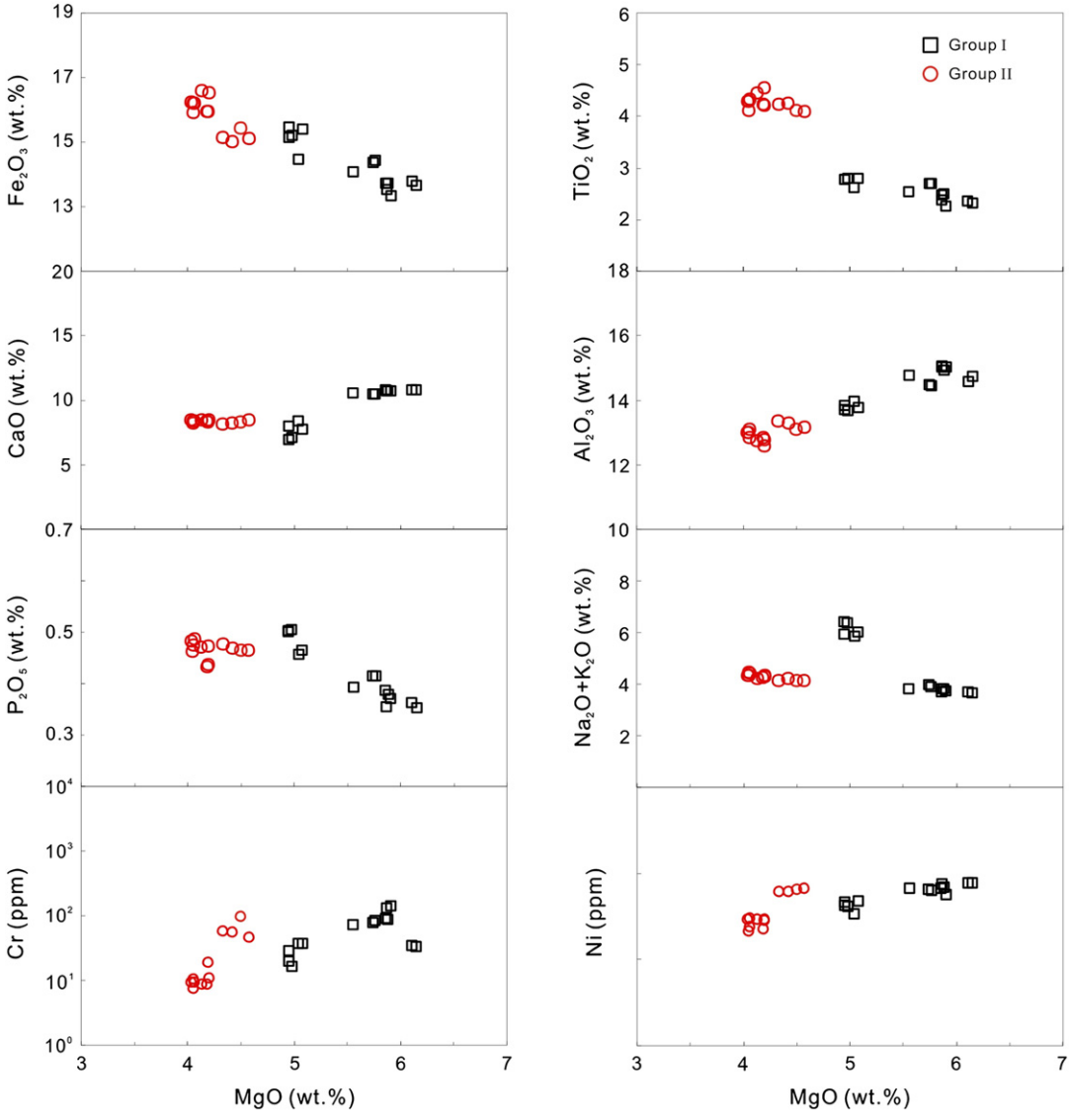

Fig. 5. Fenner diagrams for the Wuding mafic dykes.

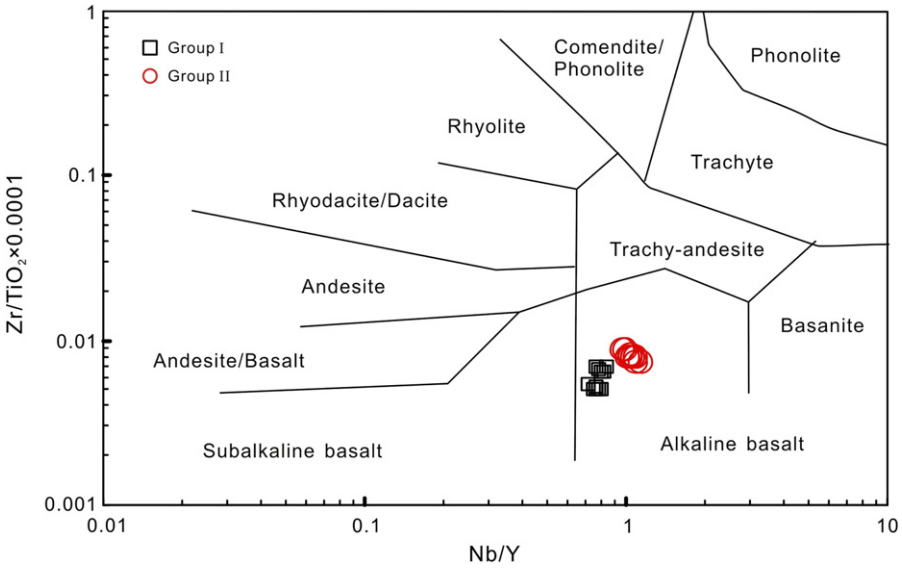

Fig. 6. Nb/Y vs. Zr/TiO_2 diagram for classification of the Wuding mafic dykes (Winchester and Floyd, 1976).

Ta of the Group I rocks is also due to AFC process, whereas the magmas parental to the Group II rocks seems to be mainly produced by slight wallrock assimilation and significant fractional crystallization of magmas parental to the Group I dykes (Fig. 10).

5.2.2. Primary magma and mantle source

The $(^{87}Sr/^{86}Sr)_I$ and $\varepsilon_{Nd}(T)$ arrays defined by the samples from Wuding (see Fig. 8) indicate a mantle source that is isotopically identical to the least contaminated picrites in the Emeishan LIP (Chung and Jahn, 1995; Zhang et al., 2006; Wang et al., 2007) and also similar to those of oceanic hotspots (calculated to 260 Ma). Moreover, the multi-element and REE patterns (Fig. 7a) as well as incompatible element ratios (Fig. 7b) of these mafic dykes are similar to those of the Emeishan picrites, suggesting an OIB-type mantle source. The Ce/Pb, Nb/Th, Nb/U and Th/La ratios for most samples are near or within the ranges for OIB (Sun and McDonough, 1989), similar to those of high-Ti basalts in the Binchuan section, SW China (e.g., Xu et al., 2001; Xiao et al., 2004). In addition, the OIB-like geochemical signatures are also supported by high LILE/LREE and LREE/HFSE ratios described above.

Among the Wuding mafic rocks, sample WD1305 is one of the least-evolved samples, having the lowest $(^{87}Sr/^{86}Sr)_I$ ratio and relative high MgO (5.91%) and $\varepsilon_{Nd}(T)$ value (2.6) which was not effected by plagioclase accumulation insignificant as no obviously positive anomalies of Sr. With this sample, we calculated the major element composition of the parental magma by using a numerical procedure to strip off the chemical effects of olivine crystallization. Equilibrium olivine is added at 1% increments until the resulting basaltic magma obtained an Mg# of 0.7 (Fram and Lesher, 1997) and equilibrated with Fo 89–91 olivine, using $Kd = (FeO/MgO)^{Ol}/(FeO/MgO)^{L} = 0.3$ (Roeder and Emslie, 1970) and assuming Fe^{2+}/total Fe = 0.85. After removing the effect of ~26% olivine crystallization, the primary magma contains ~48% SiO_2, ~19% MgO and ~10% FeO^T, which is similar to the primitive magmas for the high-Ti basalts and Fe–Ti rich mafic intrusions in the ELIP, such as those calculated by Ali et al. (2010), and may have had been Fe-picrites as reported by Zhang et al. (2006, 2008) and Wang et al. (2007).

The $\varepsilon_{Nd}(T)$ values of the mafic dykes those vary from +0.87 to +3.7 together with evidences for crustal contamination suggest that their primary melts were originated by partial melting of a long-term depleted mantle source and subsequent assimilation and fractional crystallization processes. Their moderately sloping chondrite-normalized HREE patterns (Fig. 7a) and relatively high $(Gd/Yb)_{PM}$ ratios (2.25–3.37) indicate the presence of residual garnet during partial melting because

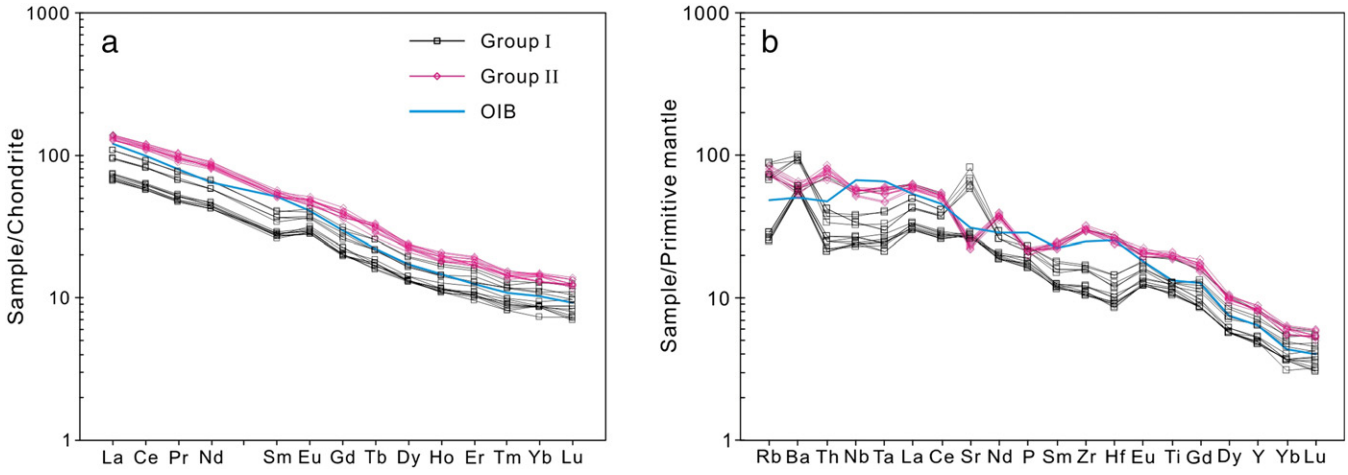

Fig. 7. a) Chondrite-normalized REE patterns of the Wuding mafic dykes, with normalizing values from Boynton (1984). b) Primitive mantle-normalized incompatible trace element spider diagram for the Wuding mafic dykes, with normalizing values from Sun and McDonough (1989). OIB data taken from Sun and McDonough (1989).

Table 3
Sr-Nd isotopic compositions of the Wuding dykes.

Sample	Rb (ppm)	Sr (ppm)	$^{87}Sr/^{86}Sr \pm 2\sigma$	$(^{87}Sr/^{86}Sr)_I$	Sm (ppm)	Nd (ppm)	$^{143}Nd/^{144}Nd \pm 2\sigma$	$(^{143}Nd/^{144}Nd)_I$	$\varepsilon_{Nd}(T)$
Group I									
WD1302	54.6	1440	0.708094 ± 27	0.70769	7.91	26.9	0.512612 ± 26	0.512311	+0.1
WD1305	17.6	605	0.705091 ± 14	0.70478	5.43	26.7	0.512643 ± 15	0.512435	+2.6
WD1307	18.2	574	0.705433 ± 18	0.70509	5.49	18.9	0.512606 ± 9	0.512308	+0.1
WD1401	44.3	1390	0.708010 ± 10	0.70767	7.09	35.0	0.512628 ± 8	0.512408	+2.0
WD1412	16.6	583	0.705196 ± 17	0.70489	5.10	25.1	0.512615 ± 24	0.512422	+2.3
WD1414	18.3	555	0.705726 ± 19	0.70517	5.32	26.7	0.512621 ± 10	0.512463	+3.1
Group II									
WD1308	46.7	474	0.706611 ± 14	0.70556	10.7	39.3	0.512628 ± 8	0.512349	+0.9
WD1402	53.8	543	0.706842 ± 36	0.70578	11.1	53.3	0.512615 ± 12	0.512407	+2.0
WD1403	53.2	527	0.706846 ± 13	0.70577	10.8	52.4	0.512621 ± 13	0.512476	+3.4
WD1407	46.3	511	0.706880 ± 16	0.70591	10.1	50.5	0.512688 ± 33	0.512439	+2.7
WD1417	47.4	460	0.706528 ± 20	0.70542	10.3	50.3	0.512644 ± 18	0.512496	+3.8

Chondrite uniform reservoir (CHUR) values ($^{87}Rb/^{86}Sr = 0.0847$, $^{87}Sr/^{86}Sr = 0.7045$, $^{147}Sm/^{144}Nd = 0.1967$, $^{143}Nd/^{144}Nd = 0.512638$) are used for the calculation. $\lambda_{Rb} = 1.42 \times 10^{-11}$ year^{-1} (Steiger and Jäger, 1977); $\lambda_{Sm} = 6.54 \times 10^{-12}$ year^{-1} (Lugmair and Harti, 1978). The $(^{87}Sr/^{86}Sr)_I$, $(^{143}Nd/^{144}Nd)_I$ and $\varepsilon_{Nd}(T)$ were calculated using the age of 260 Ma.

garnet has high partition coefficients for HREE. In addition, these lavas have relatively high Tb/Yb ratios, which generally increase with increasing Sm (Fig. 9b). Such high Tb/Yb ratios also suggest garnet in the partial melting residue, a feature of melting at greater depths.

Sm and Yb are compatible with garnet but not with olivine or plagioclase, thus the plot of Sm/Yb versus La/Sm and Gd/Yb versus La/Sm diagrams can be used to model the source characteristics in terms of mineralogy (Aldanmaz et al., 2000) (Fig. 11). Partial melting of a spinel–lherzolite source will result in a constant Gd/Yb and Sm/Yb ratios, whereas the La/Sm ratios should decrease with increasing degrees of melting (Aldanmaz et al., 2000). Therefore, partial melts derived from spinel–lherzolite sources should define melting trends sub-parallel to, and nearly coincident with, a spinel–lherzolite melting trend defined by depleted and enriched source compositions (Green, 2006). On the other hand, Sm/Yb and La/Sm ratios may be elevated during fractional crystallization of mafic minerals and plagioclase, thus, the low Gd/Yb and La/Sm ratios would be approaching to initial ratios of the primary magmas relatively. The Wuding mafic rocks are displaced from the mantle array and plot between the melting trajectories for garnet- and garnet + spinel–lherzolite, moreover, crustal contamination will enhance the Sm/Yb and La/Sm ratios, the original melts from which these samples were derived should plot much closer to garnet–lherzolite melting curve, indicating that the Wuding rocks was derived from a garnet + spinel-bearing mantle with more garnet than spinel.

The degree of partial melting to form the high-Ti basaltic rocks is constrained by the high concentrations of incompatible elements of the rocks. The high $(Sm/Yb)_{PM}$ ratios (3.09 to 5.14) of the Wuding dykes indicate small degrees of partial melting of a relatively deep mantle source (Fig. 7). The degree of partial melting was probably <10% for the parental magmas of the high-Ti basalts on the basis of Sm versus Sm/Yb and La/Sm versus Sm/Yb (Fig. 11).

The $(^{87}Sr/^{86}Sr)_I$ and $\varepsilon_{Nd}(T)$ data for these samples plot into the field of the Emeishan flood basalts, and extend from the OIB-like compositions toward the enriched quadrant (Fig. 8). This suggests a contribution from an enriched lithospheric component. The

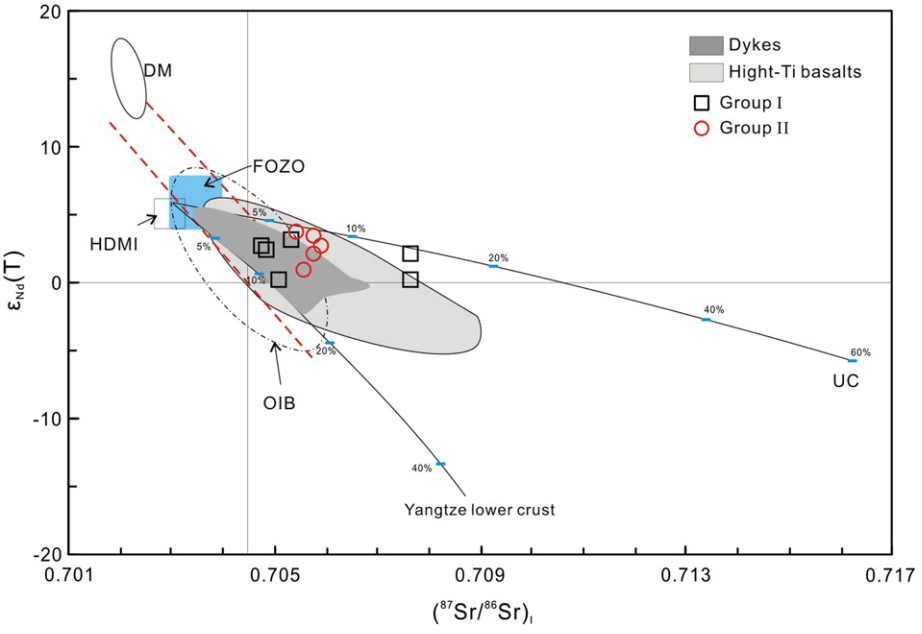

Fig. 8. $\varepsilon_{Nd}(T)$ vs. initial $^{87}Sr/^{86}Sr$ plot for the Permian mafic dykes in the Wuding area, SW China. Emeishan high-Ti basalt data are taken from Xu et al. (2001), Xiao et al. (2004), Song et al. (2004, 2008), Wang et al. (2007), Fan et al. (2008), Qi et al. (2008), Qi and Zhou (2008), and Shellnutt et al. (2008). Emeishan dyke data taken from Guo et al. (2004), Zhou et al. (2006b), Zi et al. (2008), Shellnutt et al. (2008), Shellnutt and Jahn (2011), and Li et al. (2015b). The Yangtze lower crust represented by the Kongling granitic gneiss is after Gao et al. (1999) and Ma et al. (2000), upper crust (UC) is from Rudnick and Gao (2003). HIMU range is taken from Zindler and Hart (1986). FOZO range is taken from Hart et al. (1992) and Campbell (2007).

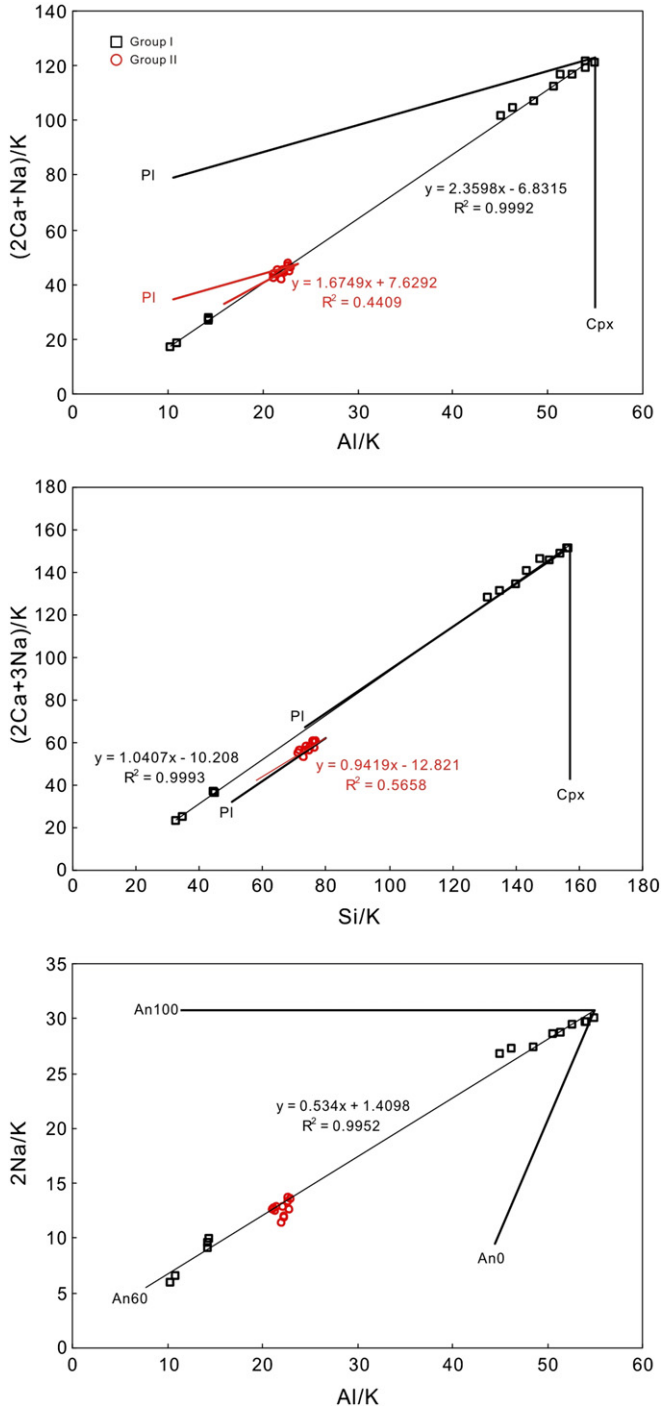

Fig. 9. Elemental ratio diagrams of (a) Al/K versus (2Ca + Na)/K and (b) Si/K versus (2Ca + 3Na)/K for the Wuding mafic dykes.

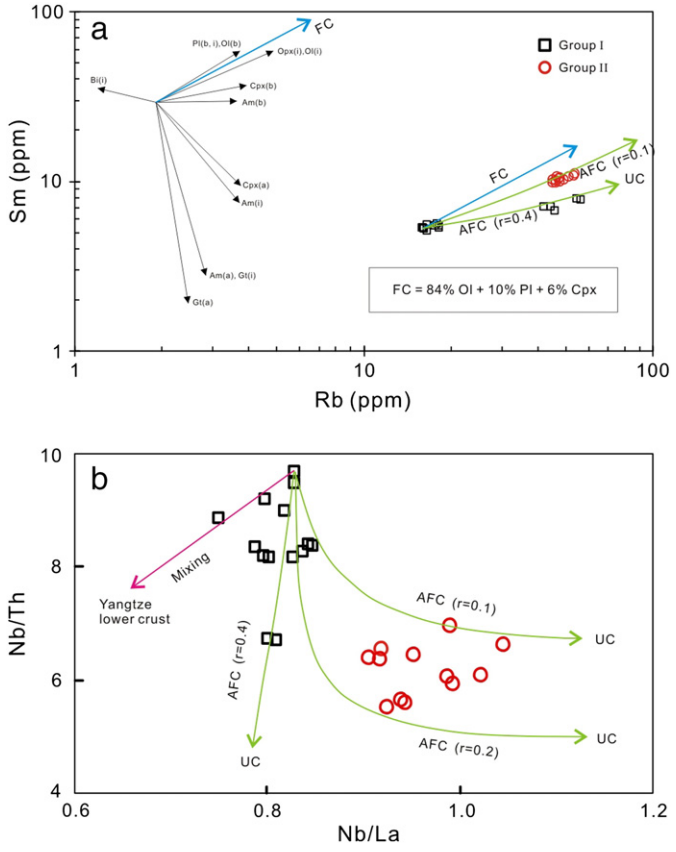

Fig. 10. Plots of (a) Sm vs. Rb and (b) Nb/Th vs. Nb/La for samples of the Wuding mafic dykes. The Yangtze lower crust represented by the Kongling granitic gneiss is after Gao et al. (1999) and Ma et al. (2000), upper crust (UC) is from Rudnick and Gao (2003). Theoretical linear trends for a particular mineral or relevant mineral assemblages in (a) are for 50% crystallization of single phases and phase combinations. Partition coefficients used for the modeling are from Keskin et al. (1998). r = ma/mc, where ma is the amount of assimilated material and mc is the amount of crystallized material. am: amphibole, Ol: olivine, Cpx: clinopyroxene, Opx: orthopyroxene, Pl: plagioclase, Bi: biotite, Gt: garnet; b: basic; i: intermediate; a: acid.

previously metasomatized SCLM with arc-like geochemical signatures generated arc-type low-Ti magma when the Emeishan plume impinged onto the western Yangtze Block (Xiao et al., 2004). However, this signature is not observed in the samples from the Wuding mafic dykes, although some samples show slight Nb–Ta depletion. The generally depleted Sr–Nd isotopic signatures also support the proposal that the SCLM was not significantly involved in the formation and evolution of these basaltic magmas. In this regard, there may be no significant contribution of SCLM or subducted sediment-derived materials in the source region.

5.3. Implications for the formation of Fe-Ti rich mafic rocks in the ELIP

Previous studies paid some attention to the abundant ultramafic–mafic dykes in Panxi region (e.g., Guo et al., 2004; Zhou et al., 2006b; Zi et al., 2008; Shellnutt et al., 2008; Shellnutt and Jahn, 2011), however, there is a lack of systematic and comparative studies for the region. As discussed above, these mafic dykes have ages identical to those of the associated volcanics and layered intrusions in ELIP, and they are compositionally and isotopically comparable with the Emeishan flood basalts. Therefore, the temporal and spatial association and petrogenetic link between the mafic dykes in the Panxi region and the Emeishan basalts suggest that these dykes are the products of the same magmatic event for this large igneous province, which formed a suite of flood basalts and associated Fe–Ti mineralized mafic rocks.

The increasing enrichment of Fe and Ti from the Group I to the Group II dykes is attributed to a fractional crystallization process, suggesting that the concentrating process of Fe and Ti in the mafic rocks in the Wuding area may be an epitome of the enrichment of Fe and Ti in mafic rocks of the ELIP. For instance, just as the formation of the Wuding dykes, under relative low fO_2 (magnetite may crystallize at an early stage from magma with a relatively high fO_2 (Ganino et al. 2008; Pang et al. 2010; Bai et al. 2012; Fan et al., 2014), after crystallization of olivine, plagioclase and clinopyroxene from an original high-Ti basaltic parental magma (e.g., magma parent to the Group I dykes in the Wuding area), the residual liquid (e.g., magma parent to the Group II dykes in

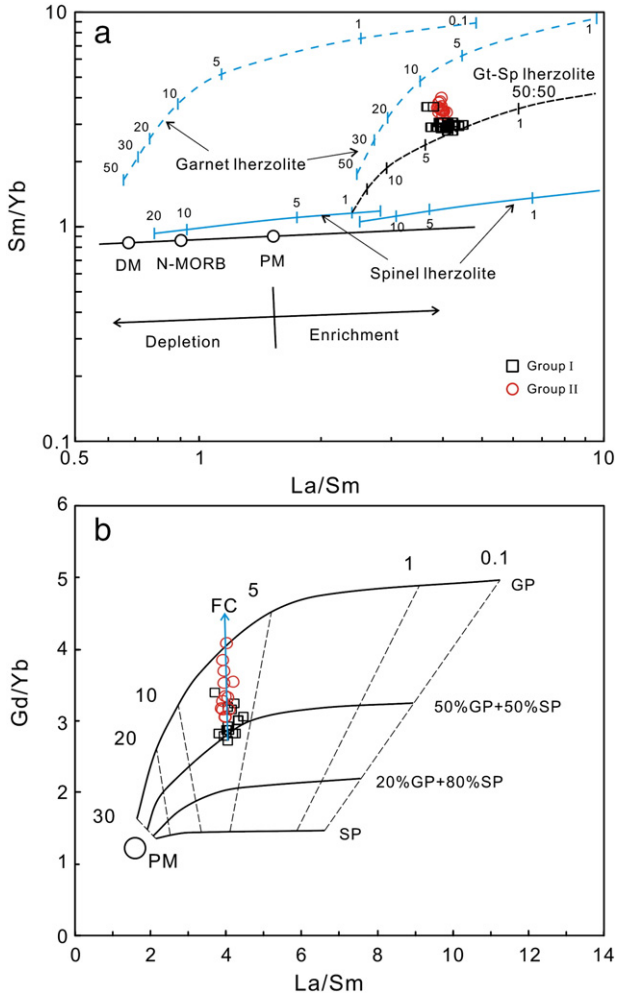

Fig. 11. Plots of (a) Sm/Yb vs. La/Sm and (b) Gd/Yb vs. La/Sm for samples of the Wuding mafic dykes. The referred melt curves are after Aldanmaz et al. (2000). The assumed proportion of partial melting is 10–50% Ol + 30–50% Opx + 0–40% Cpx + 0–20% garnet for garnet peridotite (Walter, 1998) and is 20–35% Ol + 20% Opx + 20% Cpx + 5–20% spinel (Kinzler, 1997). Primitive mantle (PM) and N-MORB compositions are from Sun and McDonough (1989), upper crust (UC) is from Rudnick and Gao (2003). FC: 84% Ol + 10% Pl + 6% Cpx. GP: garnet peridotite, SP: spinel peridotite, Ol: olivine, Opx: orthopyroxene, and Cpx: clinopyroxene.

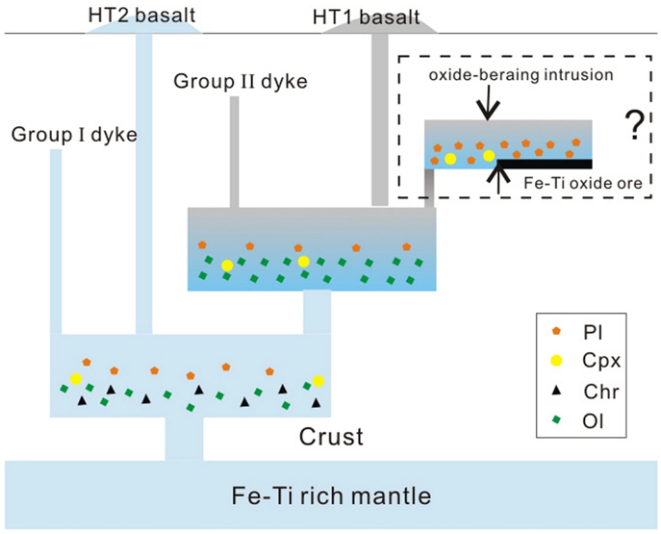

Fig. 12. An integrated model for the ELIP magmatism that produced the HT1 and HT2 basalts and the Group I and Group II mafic dykes and associated Fe–Ti oxide ore deposits. The magmas parental to the HT2 basalts and the Group I dykes experienced fractionation of olivine and chromite, whereas the magmas parental to the HT1 basalts and the Group II dykes are produced by wallrock assimilation and fractional crystallization of magma parental to the HT2 basalts and Group I rocks. Pl = plagioclase; Cpx = clinopyroxene, Ol = olivine, and Chr = chromite.

the Wuding area) will be more enriched in incompatible elements Fe, and Ti. The Fe-Ti deposits in the ELIP can be divided into two groups based on their compositions and stratigraphy. For example, the deposits at Hongge and Xinjie may have originated from more primitive parental magmas but were certainly subject to open system magmatic processes (i.e. recharge, assimilation). However, the Panzhihua, Baima and Taihe deposits were likely originated from more evolved parental magmas (i.e. basaltic) and comparatively less influenced by open system magmatic process. Then, the fractional crystallization processes that cause the enrichment of Fe and Ti from the Group I to the Group II dykes may also exist in the formation of the Panzhihua, Baima and Taihe complexes (Zhou et al., 2005; Ganino et al., 2008; Pang et al., 2008a,b, 2009, 2010, 2013; Shellnutt et al., 2009, 2011; Zhang et al., 2009; Shellnutt and Jahn, 2010; Zhong et al., 2011; Song et al., 2013).

The widespread HT2 basalts may have formed by fractionation of Fe-picritic magmas occurred at the depth, the evolved magmas could also be emplaced in shallower magma chambers as HT2 dykes (Fig. 12). Many ore-hosting intrusions are gabbroic in composition and formed from more evolved magmas. For instance, in the Panzhihua and Baima intrusions, the massive Fe–Ti oxide ore bodies are hosted in their lower parts where the majority of rocks are gabbroic in composition, though there is also evidence suggesting that the magma emplaced and crystallized the intrusions were moderately evolved, rather than highly evolved (see Pang et al., 2009 and references therein). Such evolved magmas can be produced by wallrock assimilation and fractional crystallization of melts similar to the parent magma of the Group I rocks (Figs. 10 and 12).

6. Conclusions

(1) The new SIMS baddeleyite U-Pb ages show that the Wuding mafic dykes, including the Group I and the Group II diabases, are consistent with those of ELIP plutonic bodies and the associated volcanic rocks. The mafic dykes have compositions and isotopic signatures similar to those of the basalts in the ELIP, strongly suggesting that they are all part of the same magmatic event at ~260 Ma.

(2) The primary melts of the dykes in Wuding were originated by partial melting of a long-term depleted OIB-like mantle source and subsequent assimilation and fractional crystallization processes. The widespread HT2 basalts may have formed by fractionation of Fe-picritic magmas occurred at the depth, the evolved magmas could also be emplaced in shallower magma chambers as HT2 dykes.

(3) The increasing enrichment of Fe and Ti from the Group I to the Group II rocks were attributed to a fractional crystallization process which may be an epitome of enrichment of Fe and Ti in the Fe–Ti rich mafic intrusions of the ELIP.

Acknowledgements

We appreciate Q.L. Li, G.Q. Tang, and X.X. Lin for their assistances in SIMS dating, J. Hu, G.P. Bao and Y. Huang for trace element analyses by ICP-MS, F. Xiao, and X.B. Li for Sr–Nd isotope analyses by TIMS. The paper was reviewed by Drs. J. Gregory Shellnutt and Kwan-Nang Pang whose comments significantly improved the manuscript. This work is supported by the Strategic Priority Research Program of the Chinese Academy of Sciences (Grant No.XDB18030204), the National Science Foundation of China (Grants 41403044, 41572074, and 41430315).

Appendix A. The compositions of equilibrium plagioclases calculated by using COMAGMAT–3.5

Sample	Temp.C	lg fO_2	Ab	An	SiO_2	TiO_2	Al_2O_3	FeO	MnO	MgO	CaO	Na_2O	K_2O
WD1301	1064.47	−15.66	34.12	60.78	49.82	2.83	13.92	13.87	0.26	5.03	6.98	2.84	3.68
WD1302	1070.07	−15.60	33.30	61.87	49.98	2.82	13.88	13.65	0.24	5.06	7.17	2.98	3.47
WD1401	1099.62	−15.22	41.16	55.15	49.77	2.65	14.16	12.98	0.22	5.12	8.48	3.22	2.71
WD1410	1092.53	−15.28	34.47	61.85	49.37	2.83	13.99	13.83	0.23	5.16	7.80	3.42	2.66
WD1411	1095.07	−15.27	36.95	59.35	49.45	2.82	14.02	13.58	0.23	5.03	8.10	3.34	2.68
WD1303	1178.86	−13.98	67.28	31.74	48.92	2.35	14.91	12.26	0.20	6.24	10.88	2.92	0.76
WD1304	1174.98	−14.04	65.96	33.01	48.91	2.38	14.75	12.37	0.21	6.19	10.88	2.94	0.79
WD1305	1184.89	−13.92	68.41	30.62	49.13	2.29	15.23	11.95	0.20	5.99	10.86	2.99	0.77
WD1306	1185.05	−13.91	68.68	30.36	48.97	2.40	15.21	12.14	0.20	5.95	10.86	2.96	0.76
WD1307	1177.7	−14.03	66.29	32.63	49.07	2.59	15.02	12.69	0.21	5.66	10.68	3.02	0.85
WD1412	1181.61	−13.96	67.23	31.73	48.55	2.53	15.14	12.30	0.21	5.97	10.84	3.04	0.82
WD1413	1185.79	−13.91	68.26	30.74	48.43	2.51	15.25	12.31	0.20	5.94	10.93	3.04	0.79
WD1414	1168.8	−14.14	63.21	35.66	48.40	2.72	14.65	12.97	0.21	5.85	10.62	3.07	0.86
WD1415	1168.18	−14.15	62.72	36.10	48.38	2.74	14.67	12.89	0.22	5.83	10.62	3.11	0.89
WD1308	1110.29	−14.97	51.09	46.54	50.62	4.16	13.29	13.92	0.18	4.57	8.41	2.56	1.64
WD1309	1112.03	−14.96	52.06	45.56	50.67	4.15	13.33	13.63	0.18	4.65	8.56	2.54	1.64
WD1402	1107.37	−15.08	45.77	51.72	50.46	4.17	13.20	14.33	0.20	4.12	8.33	2.80	1.72
WD1403	1105.11	−15.10	45.56	51.96	50.49	4.27	12.95	14.36	0.21	4.27	8.41	2.71	1.67
WD1404	1108.45	−15.05	47.01	50.61	50.34	4.30	13.05	14.37	0.21	4.26	8.51	2.71	1.62
WD1405	1104.76	−15.10	44.75	52.80	49.64	4.63	12.77	14.90	0.21	4.27	8.54	2.72	1.63
WD1406	1107.17	−15.08	45.44	52.07	49.96	4.40	13.04	14.60	0.20	4.14	8.49	2.79	1.69
WD1407	1109.17	−15.02	47.02	50.65	49.58	4.53	12.93	14.95	0.22	4.20	8.61	2.70	1.57
WD1408	1112.47	−15.00	47.19	50.49	49.80	4.36	13.19	14.65	0.21	4.11	8.59	2.82	1.59
WD1409	1112.86	−14.97	48.09	49.61	49.88	4.36	13.29	14.60	0.21	4.13	8.46	2.79	1.59
WD1416	1112.99	−14.95	51.14	46.54	50.78	4.30	13.46	13.52	0.18	4.50	8.35	2.64	1.61
WD1417	1111.74	−14.95	53.20	44.40	50.87	4.29	13.53	13.69	0.15	4.40	8.23	2.51	1.69

The Fe^{2+}/FeO is given as 0.99 in the COMAGMAT–3.5 (Ariskin, 1999) calculation.

References

Aldanmaz, E., Pearce, J.A., Thirlwall, M.F., Mitchell, J.G., 2000. Petrogenetic evolution of late Cenozoic, post-collision volcanism in western Anatolia, Turkey. J. Volcanol. Geotherm. Res. 102, 67–95.

Ali, J.R., Fitton, J.G., Herzberg, C., 2010. Emeishan large igneous province (SW China) and the mantle-plume up-doming hypothesis. J. Geol. Soc. 167, 953–959.

Ali, J.R., Thompson, G.M., Zhou, M.F., Song, X.Y., 2005. Emeishan large igneous province, SW China. Lithos 79, 475–489.

Anh, T.V., Pang, K.N., Chung, S.L., Lin, H.M., Hoa, T.T., Anh, T.T., Yang, H.J., 2011. The Song Da magmatic suite revisited: a petrologic, geochemical and Sr–Nd isotopic study on picrites, flood basalts and silicic volcanic rocks. J. Asian Earth Sci. 42, 1341–1355.

Ariskin, A.A., 1999. Phase equilibria modeling in igneous petrology: use of COMAGMAT model for simulating fractionation of ferro-basaltic magmas and the genesis of high-alumina basalt. J. Volcanol. Geotherm. Res. 90, 115–162.

Bai, Z.J., Zhong, H., Naldrett, A.J., Zhu, W.G., Xu, G.W., 2012. Whole-rock and mineral composition constraints on the genesis of the giant Hongge Fe-Ti-V oxide deposit in the Emeishan large igneous province, southwest China. Econ. Geol. 107, 507–524.

Boynton, W.V., 1984. Geochemistry of the rare earth elements: meteorite studies. In: Henderson, P. (Ed.), Rare Earth Element Geochemistry. Elsevier, pp. 63–114.

Campbell, I.H., 2007. Testing the plume theory. Chem. Geol. 241, 153–176.

Chung, S.L., Jahn, B.M., 1995. Plume-lithosphere interaction in generation of the Emeishan flood basalts at the Permian-Triassic boundary. Geology 23, 889–892.

Fan, H.P., Zhu, W.G., Zhong, H., Bai, Z.J., He, D.F., Ye, X.T., Chen, C.J., Cao, C.Y., 2014. Platinum-group element geochemistry of the Zhuqing Fe–Ti–V oxide ore-bearing mafic intrusions in western Yangtze Block, SW China: control of platinum-group elements by magnetite. Mineral. Petrol. 109, 419–438.

Fan, W.M., Wang, Y.J., Peng, T.P., Miao, L.C., Guo, F., 2004. Ar–Ar and U–Pb geochronology of Late Paleozoic basalts in western Guangxi and its constraints on the eruption age of Emeishan basalt magmatism. Chin. Sci. Bull. 49, 318–2327.

Fan, W., Zhang, C., Wang, Y., Guo, F., Peng, T., 2008. Geochronology and geochemistry of Permian basalts in western Guangxi Province, southwest China: evidence for plume-lithosphere interaction. Lithos 102, 218–236.

Fram, M.S., Lesher, C.E., 1997. Generation and polybaric differentiation of Greenland Early Tertiary flood basalts. J. Petrol. 38, 231–275.

Ganino, C., Arndt, N.T., Zhou, M.-F., Gaillard, F., Chauvel, C., 2008. Interaction of magma with sedimentary wall rock and magnetite ore genesis in the Panzhihua mafic intrusion, SW China. Mineral. Deposita 43, 677–694.

Gao, S., Ling, W., Qiu, Y., Lian, Z., Hartmann, G., Simon, K., 1999. Contrasting geochemical and Sm–Nd isotopic compositions of Archean metasediments from the Kongling high-grade terrain of the Yangtze craton: evidence for cratonic evolution and redistribution of REE during crustal anatexis. Geochim. Cosmochim. Acta 63, 2071–2088.

Green, N.L., 2006. Influence of slab thermal structure on basalt source regions and melting conditions: REE and HFSE constraints from the Garibaldi volcanic belt, northern Cascadia subduction system. Lithos 87, 23–49.

Guo, F., Fan, W., Wang, Y., Li, C., 2004. When did the Emeishan mantle plume activity start? Geochronological and geochemical evidence from ultramafic-mafic dikes in southwestern China. Int. Geol. Rev. 46, 226–234.

Han, W., Luo, J.H., Fan, J.L., Cao, Y.Z., Zhang, J.Y., 2009. Late Permian diabase in Luodian, southeastern Guizhou, and its tectonic significances. Geogr. Rev. 55, 795–803 (in Chinese with English abstract).

Hart, S.R., Hauri, E.H., Oschmann, L.A., Whitehead, J.A., 1992. Mantle plumes and entrainment: isotopic evidence. Science 256, 517–520.

Jin, Y., Shang, J., 2000. The Permian of China and its interregional correlation. In: Yin, H., Dickins, J.M., Shi, G.R., Tong, J. (Eds.), Permian–Triassic Evolution of Tethys and Western Circum-PacificDevelopments in Palaeontology and Stratigraphy Vol. 18. Elsevier Press, Amsterdam, pp. 71–98.

Keskin, M., Pearce, J.A., Mitchell, J.G., 1998. Volcano-stratigraphy and geochemistry of collision-related volcanism on the Erzurum-Kars Plateau, northeastern Turkey. J. Volcanol. Geotherm. Res. 85, 355–404.

Kinzler, R.J., 1997. Melting of mantle peridotite at pressures approaching the spinel to garnet transition: application to mid-ocean ridge basalt petrogenesis. J. Geophys. Res. 102, 853–874.

Lai, S.C., Qin, J.F., Li, Y.F., Li, S.Z., Santosh, M., 2012. Permian high Ti/Y basalts from the eastern part of the Emeishan Large Igneous Province, southwestern China: petrogenesis and tectonic implications. J. Asian Earth Sci. 47, 216–230.

Li, H.B., Zhang, Z.C., Ernst, R.E., Lü, L., Santosh, M., Zhang, D.Y., Cheng, Z.G., 2015a. Giant radiating mafic dyke swarm of the Emeishan Large Igneous Province: identifying the mantle plume centre. Terra Nova 27, 247–257.

Li, H.B., Zhang, Z.C., Li, Y.S., 2015b. Geochronology and geochemistry of the Late Permian intermediary–mafic intrusions in Fumin, Yunnan province: implications for the magmatism of Emeishan large igneous province. Acta Geol. Sin. 89, 18–36 (in Chinese with English abstract).

Li, H.B., Zhang, Z.C., Lü, L., Li, Y.S., 2012. Geochronology, geochemistry and geological significances of the Permian basic dykes in Mianning, Sichuan Province. Geol. Rev. 58, 952–964 (in Chinese with English abstract).

Li, Q.L., Li, X.H., Liu, Y., Tang, G.Q., Yang, J.H., Zhu, W.G., 2010. Precise U-Pb and Pb-Pb dating of Phanerozoic baddeleyite by SIMS with oxygen flooding technique. J. Anal. Spectrom. 25, 1107–1113.

Li, X.H., Li, Z.X., Sinclair, J.A., Li, W.X., Carter, G., 2006. Revisiting the "Yanbian Terrane:" implications for Neoproterozoic tectonic evolution of the western Yangtze block, South China. Precambrian Res. 151, 14–30.

Li, Z.X., Li, X.H., Kinny, P.D., Wang, J., Zhang, S., Zhou, H., 2003. Geochronology of Neoproterozoic syn-rift magmatism in the Yangtze craton, south China and correlations with other continents: evidence for a mantle superplume that broke up Rodinia. Precambrian Res. 122, 85–109.

Lugmair, G.W., Harti, K., 1978. Lunar initial $^{143}Nd/^{144}Nd$: differential evolution of the lunar crust and mantle. Earth Planet. Sci. Lett. 39, 349–357.

Ma, C., Ehlers, C., Xu, C., Li, Z., Yang, K., 2000. The roots of the Dabieshan ultrahigh-pressure metamorphic terrane: constraints from geochemistry and Nd–Sr isotope systematics. Precambrian Res. 102, 279–301.

Munteanu, M., Yao, Y., Wilson, A.H., Chunnett, G., Luo, Y., He, H., Cioacă, M., Wen, M., 2013. Panxi region (South-West China): tectonics, magmatism and metallogenesis. A review. Tectonophysics 608, 51–71.
Pang, K.N., Li, C., Zhou, M.F., Ripley, E.M., 2008a. Abundant Fe-Ti oxide inclusions in olivine from the Panzhihua and Hongge layered intrusions, SW China: evidence for early saturation of Fe-Ti oxides in ferrobasaltic magma. Contrib. Mineral. Petrol. 156, 307–321.
Pang, K.N., Li, C., Zhou, M.F., Ripley, E.M., 2009. Mineral compositional constraints on petrogenesis and oxide ore genesis of the late Permian Panzhihua layered gabbroic intrusion, SW China. Lithos 110, 199–214.
Pang, K.N., Zhou, M.F., Lindsley, D., Zhao, D., Malpas, J., 2008b. Origin of Fe-Ti oxide ores in mafic intrusions: evidence from the Panzhihua intrusion, SW China. J. Petrol. 49, 295–313.
Pang, K.N., Zhou, M.F., Qi, L., Chung, S.L., Chu, C.H., Lee, H.Y., 2013. Petrology and geochemistry at the LZ-MZa transition of the Panzhihua intrusion: implications for differentiation and oxide ore genesis. Geosci. Front. 4, 517–533.
Pang, K.N., Zhou, M.F., Qi, L., Shellnutt, J.G., Wang, C.Y., Zhao, D., 2010. Magmatic Fe-Ti-V oxide deposits in the Emeishan large igneous province, SW China. Lithos 119, 123–136.
Qi, L., Hu, J., Grégoire, D.C., 2000. Determination of trace elements in granites by inductively coupled plasma mass spectrometry. Talanta 51, 507–513.
Qi, L., Wang, C.Y., Zhou, M.-F., 2008. Controls on the PGE distribution of Permian Emeishan alkaline and peralkaline volcanic rocks in Longzhoushan, Sichuan Province, SW China. Lithos 106, 222–236.
Qi, L., Zhou, M.-F., 2008. Platinum-group elemental and Sr-Nd-Os isotopic geochemistry of Permian Emeishan flood basalts in Guizhou Province, SW China. Chem. Geol. 248, 83–103.
Rodionov, N.V., Belyatsky, B.V., Antonov, A.V., Kapitonov, I.N., Sergeev, S.A., 2012. Comparative in-situ U–Th–Pb geochronology and trace element composition of baddeleyite and low-U zircon from carbonatites of the Palaeozoic Kovdor alkaline–ultramafic complex, Kola Peninsula, Russia. Gondwana Res. 21, 728–744.
Roeder, P.L., Emslie, R.F., 1970. Olivine–liquid equilibrium. Contrib. Mineral. Petrol. 29, 275–289.
Russell, J.K., Nicholls, J., 1988. Analysis of petrologic hypotheses with Pearce element ratios. Contrib. Mineral. Petrol. 99, 25–35.
Rudnick, R.L., Fountain, D.M., 1995. Nature and composition of the continental crust: a lower crustal perspective. Rev. Geophys. 33, 267–309.
Rudnick, R.L., Gao, S., 2003. Composition of the Continental Crust. The Crust. In: Rudnick, R.L. (Ed.)Treatise on Geochemistry Vol. 3, pp. 1–64.
Shellnutt, J.G., 2014. The Emeishan large igneous province: a synthesis. Geosci. Front. 5 (3), 369-39.
Shellnutt, J.G., Denyszyn, S., Mundil, R., 2012. Precise age determination of mafic and felsic intrusive rocks from the Permian Emeishan large igneous province (SW China). Gondwana Res. 22, 118–126.
Shellnutt, J.G., Jahn, B.M., 2010. Formation of the Late Permian Panzhihua plutonic-hypabyssal-volcanic igneous complex: implications for the genesis of Fe-Ti oxide deposits and A-type granites of SW China. Earth Planet. Sci. Lett. 289, 509–519.
Shellnutt, J.G., Jahn, B.M., 2011. Origin of Late Permian Emeishan basaltic rocks from the Panxi region (SW China): implications for the Ti-classification and spatial-compositional distribution of the Emeishan basalts. J. Volcanol. Geotherm. Res. 199, 85–95.
Shellnutt, J.G., Wang, K.L., Zellmer, G.F., Iizuka, Y., Jahn, B.M., Pang, K.N., Qi, L., Zhou, M.F., 2011. Three Fe-Ti oxide ore-bearing gabbro-granitoid complexes in the Panxi region of the Emeishan large igneous province, SW China. Am. J. Sci. 311, 773–812.
Shellnutt, J.G., Zhou, M.F., Yan, D.P., Wang, Y., 2008. Longevity of the Permian Emeishan mantle-plume (SW China): 1 Ma, 8 Ma or 18 Ma? Geol. Mag. 145, 373–388.
Shellnutt, J.G., Zhou, M.F., Zellmer, G., 2009. The role of Fe-Ti oxide crystallization in the formation of A-type granitoids with implications for the Daly gap: an example from the Permian Baima igneous complex, SW China. Chem. Geol. 259, 204–217.
Song, X.Y., Zhou, M.F., Cao, Z.M., Robinson, P., 2004. Late Permian rifting of the South China craton caused by the Emeishan mantle plume? J. Geol. Soc. Lond. 161, 773–781.
Song, X.Y., Qi, H.W., Robinson, P.T., Zhou, M.F., Cao, Z.M., Chen, L.M., 2008. Melting of the subcontinental lithospheric mantle by the Emeishan mantle plume; evidence from the basal alkaline basalts in Dongchuan, Yunnan, southwestern China. Lithos 100, 93–111.
Song, X.Y., Qi, H.W., Hu, R.Z., Chen, L.M., Yu, S.Y., Zhang, J.F., 2013. Formation of thick stratiform Fe-Ti oxide layers in layered intrusion and frequent replenishment of fractionated mafic magma: evidence from the Panzhihua intrusion, SW China. Geochem. Geophys. Geosyst. 14, 712–732.
Steiger, R.H., Jäger, E., 1977. Subcommission on geochronology: convention on the use of decay constants in geo- and cosmochronology. Earth Planet. Sci. Lett. 36, 359–362.
Sun, S.S., McDonough, W.F., 1989. Chemical and isotopic systematics of oceanic basalts: implications for mantle composition and processes. In: Saunders, A.D., Norry, M.J. (Eds.), Magmatism in the Ocean Basins. Geological Society, London Special Publications Vol. 42, pp. 313–345.
Tao, Y., Li, C., Hu, R.Z., Ripley, E.M., Du, A.D., Zhong, H., 2007. Petrogenesis of the Pt–Pd mineralized Jinbaoshan ultramafic intrusion in the Permian Emeishan large igneous province, SW China. Contrib. Mineral. Petrol. 153, 321–337.
Walter, M.J., 1998. Melting of garnet peridotite and the origin of komatiite and depleted lithosphere. J. Petrol. 39, 29–60.
Wang, C.Y., Zhou, M.F., Qi, L., 2007. Permian flood basalts and mafic intrusions in the Jinping (SW China)–Song Da (northern Vietnam) district: mantle sources, crustal contamination and sulfide segregation. Chem. Geol. 243, 317–343.
Winchester, J.A., Floyd, P.A., 1976. Geochemical magma type discrimination: application to altered and metamorphosed igneous rocks. Earth Planet. Sci. Lett. 45, 326–336.
Wingate, M.T.D., Compston, W., 2000. Crystal orientation effects during ion microprobe U-Pb analysis of baddeleyite. Chem. Geol. 168, 75–97.
Xiao, L., Xu, Y.G., Mei, H.J., Zheng, Y.F., He, B., Pirajno, F., 2004. Distinct mantle sources of low-Ti and high-Ti basalts from the western Emeishan large igneous province, SW China: implications for plume-lithosphere interaction. Earth Planet. Sci. Lett. 228, 525–546.
Xu, J.F., Suzuki, K., Xu, Y.G., Mei, H.J., Li, J., 2007. Os, Pb, and Nd isotope geochemistry of the Permian Emeishan continental food basalts: insights into the source of a large igneous province. Geochim. Cosmochim. Acta 71, 2104–2119.
Xu, Y.G., Chung, S.L., Jahn, B.M., Wu, G.Y., 2001. Petrologic and geochemical constraints on the petrogenesis of Permian–Triassic Emeishan flood basalts in southwestern China. Lithos 58, 145–168.
Xu, Y.G., Luo, Z.Y., Huang, X.L., He, B., Xiao, L., Xie, L.W., Shi, Y.R., 2008. Zircon U–Pb and Hf isotope constraints on crustal melting associated with the Emeishan mantle plume. Geochim. Cosmochim. Acta 72, 3084–3104.
Yin, H., Huang, S., Zhang, K., Hansen, H.J., Yang, F., Ding, M., Bie, X., Sweet, W.C., Yang, Z.Y., Dickins, J.M., Yin, H.F., 1992. The effects of volcanism of the Permo-Triassic mass extinction in South China. Permo-Triassic Events in the Eastern Tethys: Stratigraphy, Classification, and Relations with the Western TethysWorld and Regional Geology vol. 2. Cambridge University Press, Cambridge, pp. 146–157.
Zi, J., Fan, W., Wang, Y., Peng, T., Guo, F., 2008. Geochemistry and petrogenesis of the Permian mafic dykes in the Panxi region, SW China. Gondwana Res. 14, 368–382.
Zindler, A., Hart, S.R., 1986. Chemical geodynamics. Annu. Rev. Earth Planet. Sci. 14, 493–571.
Zhang, Z.C., Mahoney, J.J., Mao, J.W., Wang, F., 2006. Geochemistry of picritic and associated basalt flows of the western Emeishan flood basalt province, China. J. Petrol. 47, 1997–2019.
Zhang, Z.C., Mao, J.W., Saunders, A.D., Ai, Y., Li, Y., Zhao, L., 2009. Petrogenetic modeling of three mafic-ultramafic layered intrusions in the Emeishan large igneous province, SW China, based on isotopic and bulk chemical constraints. Lithos 113, 369–392.
Zhang, Z.C., Zhi, X.C., Chen, L., Saunders, A.D., Reichow, M.K., 2008. Re-Os isotopic compositions of picrites from the Emeishan flood basalt province, China. Earth Planet. Sci. Lett. 276, 30–39.
Zheng, L., Yang, Z., Tong, Y., Yuan, W., 2010. Magnetostratigraphic constraints on two-stage eruptions of the Emeishan continental flood basalts. Geochem. Geophys. Geosyst. 11:Q12014. http://dx.doi.org/10.1029/2010GC003267.
Zhong, H., Zhu, W.-G., 2006. Geochronology of layered mafic intrusions from the Pan-Xi area in the Emeishan large igneous province, SW China. Mineral. Deposita 41, 599–606.
Zhong, H., Qi, L., Hu, R.Z., Zhou, M.F., Gou, T.Z., Zhu, W.G., Liu, B.G., Chu, Z.Y., 2011. Timing and source constraints on the relationship between mafic and felsic intrusions in the Emeishan large igneous province. Geochim. Cosmochim. Acta 75, 1374–1395.
Zhou, M.F., Arndt, N.T., Malpas, J., Wang, C.Y., Kennedy, A.K., 2008. Two magma series and associated ore deposit types in the Permian Emeishan large igneous province, SW China. Lithos 103, 352–368.
Zhou, M.F., Ma, Y., Yan, D.P., Xia, X., Zhao, J.H., Sun, M., 2006a. The Yanbian terrane (southern Sichuan province, SW China): a Neoproterozoic arc assemblage in the western margin of the Yangtze block. Precambrian Res. 144, 19–38.
Zhou, M.F., Malpas, J., Song, X.Y., Robinson, P.T., Sun, M., Kennedy, A.K., Lesher, C.M., Keays, R.R., 2002. A temporal link between the Emeishan large igneous province (SW China) and the end-Guadalupian mass extinction. Earth Planet. Sci. Lett. 196, 113–122.
Zhou, M.F., Zhao, J.H., Qi, L., Su, W., Hu, R.Z., 2006b. Zircon U-Pb geochronology and elemental and Sr-Nd isotopic geochemistry of Permian mafic rocks in the Funing area, SW China. Contrib. Mineral. Petrol. 151, 1–19.
Zhou, M.F., Robinson, P.T., Lesher, C.M., Keays, R.R., Zhang, C.J., Malpas, J., 2005. Geochemistry, petrogenesis and metallogenesis of the Panzhihua gabbroic layered intrusion and associated Fe-Ti-V oxide deposits, Sichuan Province, SW China. J. Petrol. 46, 2253–2280.
Zhu, W.G., Zhong, H., Li, X.H., Deng, H.L., He, D.F., Wu, K.W., Bai, Z.J., 2008. SHRIMP zircon U-Pb geochronology, elemental, and Nd isotopic geochemistry of the Neoproterozoic mafic dykes in the Yanbian area, SW China. Precambrian Res. 164, 66–85.